



Scaling the failure of concrete gravity dam subjected to underwater explosion shock loading

Xieping Huang^{a,*}, Xiangzhen Kong^{b,**}, Jing Hu^c, Qin Fang^b

^a Institute of Geotechnical Engineering, Zhejiang University, Zhejiang Hangzhou, 310058, China

^b State Key Laboratory of Disaster Prevention & Mitigation of Explosion & Impact, Army Engineering University of PLA, Jiangsu Nanjing, 210007, China

^c China Institute of Water Resources and Hydropower Research, Beijing, 100048, China

ARTICLE INFO

Keywords:

Underwater explosion
Concrete gravity dam
Scaling law
Shocking wave
Centrifuge tests
Strain-rate effect

ABSTRACT

The small-scale model test is the major affordable approach to experimentally investigate concrete gravity dams against underwater explosions. However, results of the small-scale model should be properly converted to the prototype, which requires the knowledge of scaling law. This study presented the scaling of failures of concrete gravity dams against underwater explosion shock loadings through small-scale centrifuge tests and numerical simulations. The dimensional analysis-based scaling law, which was essentially the geometrical scaling law for dams and the well-known Hopkinson scaling law for underwater explosion shock loadings, was employed. According to the scaling law, a numerical scheme comprising six numerical simulations with geometrical scaling factors $\beta = 1, 1/10, 1/30, 1/50, 1/80, \text{ and } 1/100$ was devised. Results demonstrated that dams with different scaling factors exhibited essentially the same failure mode, i.e., the structural bending-induced tensile failure mode. On this basis, it was discovered that most dam dynamic responses followed the scaling law. It was also found that when the strain-rate effect was pronounced, such as in dam tensile stresses and tensile failures, the scaling law was violated. Despite the incomplete scaling law, the small-scale model tests can be used to identify the most vulnerable positions of the dam prototype.

1. Introduction

1.1. Concrete gravity dam against underwater explosion

According to the statistical report by Magnus et al. (2018), during the period of 1970–2016, more than 23,352 terrorist attacks against civilian targets worldwide occurred, with 78,772 deaths. In this circumstance, there has been increasing public and academic concern about the threat of explosion attacks on military and civilian infrastructures such as dams, bridges, tunnels, airports, subway stations, etc., especially after the event of 9/11. Dam structures are indispensable infrastructures of society used primarily for water supply, flood regulation, power generation, irrigation, and shipping. However, in extreme circumstances, such as terrorist attacks and military strikes, dam structures, due to their political and economic significance, are highly likely to encounter blast loadings. The review literature (Wang et al., 2020a; Chen et al., 2021) reported that more than ten dams were destroyed by explosions in historical wars during the 20th century. The statistics (U.S. Department of

Homeland Security, 2012) showed that up to 25 dams had encountered explosion attacks during 2001–2011.

Understanding the dynamic responses and failures of dam structures against blast loadings is a key to successful protection projects. The underwater explosion is one of the most severe scenarios the dam structures may experience. Compared to the air blast with the same explosive weight, the underwater explosion is well-known can cause significantly more severe damage to dam structures (Cole, 1948; Wang et al., 2015). Extensive attention, therefore, has been drawn to the dynamic responses and failures of concrete gravity dams subjected to underwater explosions.

For a general scientific problem, one may explore it experimentally, numerically, and/or theoretically. However, for the subject of concrete gravity dams against underwater explosions, to investigate it theoretically, if not impossible, is rather complicated, which involves the underwater explosion processes, the fluid-structure interactions, and the highly nonlinear dynamic responses of dam structures. The underwater explosion itself is also very involved, which is accompanied by complex

* Corresponding author.

** Corresponding author.

E-mail addresses: huangxieping@zju.edu.cn (X. Huang), ouckxz@163.com (X. Kong).

physical phenomena, including shock wave propagation, the expansion, contraction, collapse, and migration of gas bubble, water jet, cavitation, and so on. For these reasons, advances in theoretical investigations were rarely reported.

By contrast, with the rapid development of numerical methods and constitutive material models, relevant numerical studies were abundant. With the Coupled Lagrangian-Eulerian method or the Arbitrary Lagrangian-Eulerian method, researchers can establish the fully coupled water-air-explosive-dam numerical model and simulate the whole process of concrete gravity dams undergoing underwater explosions. On this basis, researchers (Wang and Zhang, 2014; Zhang et al., 2014; Chen et al., 2017; Li et al., 2018a; Ren and Shao, 2019) uncovered the failure modes of concrete gravity dams due to the shock wave, where the influences of water depth, explosive weight, standoff distance, detonation depth, and dam height were studied. Moreover, Saadatfar and Zahmatkesh (2018) concerned about the dam responses due to not only the shock wave but also the bubble pulse. Other than the two major phenomena, the shock wave, and the bubble pulse, some other effects that can influence the damage effect of the underwater explosion were also discussed. For instance, Li et al. (2018b) unearthed the influence of hydrostatic pressure caused by the water in the reservoir. Zhang et al. (2021) explored the role of negative pressure to highlight the need to consider the local cavitation. Besides, considering the significance of gravity effect to a concrete gravity dam, Wang et al. (2021) discovered the influence of the initial stress field of the dam. In addition, Wang et al. (2020b) focused on the evaluation method to evaluate the dam damage level. It is noted that these numerical studies were mostly conducted on the dam prototype.

In contrast to the large number of numerical studies mentioned above, the literature on experimental investigations in this field was rather sparse. Particularly, considering the large geometrical size of dam structures and the high risk due to blast loadings, full-scale experiments were usually unattainable. Only the literature review (Chen et al., 2021) briefly documented the full-scale experiments recently conducted on the Fengman old dam before its demolition in Jilin, China.

Restricted by the unaffordable costs, security concerns, and difficulties in preparations and measurements for full-scale experiments, the small-scale model test was the major feasible alternative for experimental investigations. For example, Lu et al. (2014) conducted six 1:200 small-scale model tests to uncover the dam failures due to a strong underwater shock wave generated using the hammer impact method. Severe dam failures were observed. However, the underwater shock wave generated by the hammer impact method was a plane wave that was far from a realistic spherical wave induced by the underwater explosion. The error was remarkable for near-field underwater explosions. More importantly, this kind of small-scale model test performed on the ground with normal gravity was disabled to reproduce the internal state of initial stresses of a dam prototype caused by the massive gravity of the dam and the hydrostatic pressure of the reservoir. Thus, reliable results can not be expected. Recently, with the continuous development of centrifuge apparatus and scaling theory of underwater explosions (Hu et al., 2017), researchers can investigate this subject using a centrifuge, which can effectively provide a similar gravity field to the dam prototype. Vanadit-Ellis and Davis (2010) performed a series of 1:100 centrifuge tests to discover the typical dam failure modes under different standoff distances. More recently, Huang et al. (2020a, 2022a, 2022b) conducted several small-scale centrifuge tests. Combined with numerical simulations, the dam failure modes and the underlying failure mechanisms due to the shock wave (Huang et al., 2020a, 2022b) and the effect of bubble pulse (Huang et al., 2022a) were discussed.

More small-scale model tests are highly desired. However, the validity of such kinds of tests remains to be firmly established. In other words, the results of the small-scale model should be able to infer the prototype, which requires not only the geometrical similarity between the small-scale model and the prototype but also the physical similarity of the major physical phenomena involved in the investigated problem.

The technique that relates the results of the small-scale model and the prototype is called scaling, replica scaling, modeling, or similitude. This study focuses mainly on the scaling of dynamic responses and failures of concrete gravity dams subjected to underwater explosion shock loadings.

1.2. Scaling theory

For structures against blast loadings, the major relevant parameters and the corresponding scaling factors are summarized in Table 1. These scaling factors are well-known and can be derived easily with the dimensional analysis method based on the Mass-Length-Time (MLT) basis. The scaling theory in Table 1 is straightforward, which is essentially the geometrical (replica) scaling law (Baker et al., 1973; Jones, 2012) for the structure and the Hopkinson scaling law (Baker, 1973; Alves, 2020; Ramamurthi, 2021) for the blast effect. The Hopkinson scaling law, also named as the cubic root scaling law, is the most famous method to conduct blast wave scaling, where a Hopkinson scaled distance Z is proposed and is defined as,

$$Z = \frac{R_c}{W^{1/3}} \quad (1)$$

where R_c represents the standoff distance, and W denotes the explosive weight. The Hopkinson scaling law states that self-similar blast waves are produced at an identical Hopkinson scaled distance when two explosive charges of similar geometries and explosive types but of different weights are detonated in the same fluid.

The above scaling theory was widely applied. The earlier attention was paid mainly to structures subjected to free-field air blasts. For instance, using this scaling theory, the scaling of dynamic responses of circular metal plates (Neuberger et al., 2007), thin steel plates (Snyman, 2010), square reinforced concrete slabs (Wang et al., 2012), and circular clamped plates (Noam et al., 2014) against free-field air blasts was investigated. Note that the internal air blast was more destructive compared to the free-field air blast owing to the multiple shock waves due to the reflections of the shock waves in a confined field. Then, with the same scaling theory, the scaling of dynamic responses of steel box structures (Yao et al., 2017), cylindrical lattice shell structures (Fu et al., 2018), and cabin structures (Ren et al., 2022) against internal air blasts was explored. Results in these mentioned studies demonstrated that with the scaling theory in Table 1, the scaling of dynamic responses of the different structures against air blasts can generally be implemented.

However, it is also known that for structures against blast loadings with the dimensional analysis-based scaling theory, several phenomena may not scale: (1) Gravity. For experiments conducted on the ground with normal gravity, gravitational forces can not be scaled according to the basic principles of the geometrically similar scaling law. (2) Strain-rate effect. The strain rate of the small-scale model is $1/\beta$ times enhanced compared to that of the prototype. For materials sensitive to the strain rate, this will result in $\sigma^M/\sigma^P \neq 1$, thus, violating the scaling law. (3)

Table 1
Scaling factors relating model and prototype parameters.

Parameters	Dimension	Factors
Length, L	L	$L^M/L^P = \beta$
Density, ρ	ML^{-3}	$\rho^M/\rho^P = 1$
Mass, W	M	$W^M/W^P = \beta^3$
Time, t	T	$t^M/t^P = \beta$
Displacement, δ	L	$\delta^M/\delta^P = \beta$
Strain, ϵ	-	$\epsilon^M/\epsilon^P = 1$
Stress, σ	$ML^{-1}T^{-2}$	$\sigma^M/\sigma^P = 1$
Pressure, P	$ML^{-1}T^{-2}$	$P^M/P^P = 1$
Strain rate, $\dot{\epsilon}$	T^{-1}	$\dot{\epsilon}^M/\dot{\epsilon}^P = 1/\beta$
Acceleration, a	LT^{-2}	$a^M/a^P = 1/\beta$
Energy, Q	ML^2T^{-2}	$Q^M/Q^P = \beta^3$
Fracture toughness, K_{IC}	$ML^{-1/2}T^{-2}$	$K_{IC}^M/K_{IC}^P = \beta^{1/2}$

Fracture. The fracture can not be scaled with the fracture-mechanics criteria since the fracture toughness of the small-scale model is $\beta^{1/2}$ times that of the prototype.

For gravity, if the geometrical size of the structure prototype is not very large (see Table 2) and the accelerations of structural responses are very high, then the gravitational forces are not significant and can be neglected. For the fracture, Noam et al. (2014) reported that using two alternative competing criteria instead of the fracture-mechanics criteria, the scaling of fracture and failure was possible.

The strain-rate effect, then, becomes the thorniest issue that is still unclosed. For structures under impact loads, the non-scalability due to the strain-rate effect can be addressed by correcting the impacting velocity (Oshiro and Alves, 2004; Mazzariol et al., 2016; Oshiro et al., 2017). However, for structures against blast loads, the issue is more complicated. To narrow the gap, Mazzariol et al. (2016) described an impact velocity model that was established based on a new dimensional analysis basis with the inclusion of the initial velocity v_0 , the dynamic stress σ_d , and the impact mass G . However, the damage effect of the blast shock wave acting on the structure needed to be transformed into the impact velocity, which was hard to handle and involved additional problems for the applications of this method. Kong et al. (2017) developed a corrected scaling law by taking a correction factor of impulse per unit area into consideration. The corrected scaling law was then applied to the scaling of the impact responses of steel plates against air blasts. Similar corrected scaling law was adopted by Fu et al. (2021) to scale the dynamic responses of armor steel plates subjected to air blasts. However, a particular limitation of this method was that a priori knowledge about the strain rate was required to determine the correction factor. The strain rate of the center of a plate was usually taken since the deflection of the plate center was concerned to examine the corrected scaling law. Although the plate center deflection, then, can be well scaled, this method was limiting for structures that were more complex, such as dam structures, where strain rates varied both spatially and temporally. Besides, Yao et al. (2022) proposed a new procedure to equivalent scale the dynamic responses of steel box structures subjected to internal air blasts. This method can consider the size effect of structural dimension and the strain-rate effect of materials. However, based on a dimensionless number applicable for box-shape structures against internal air blasts, the applicable scope of this method was limited. For these reasons, the mentioned studies focused mainly on the structure responses such as plate center deflections when examining the corrected scaling law. As

Table 2
Review of geometrical size of structure prototype and scaling factor in literature.

Literature	Structure type	Prototype size	Minimum Scaling factor β
Neuberger et al. (2007)	Circular metal plates	1×0.05 m (radius \times thickness)	1/10
Snyman (2010)	Thin steel plates	0.0186×0.0185 m (radius \times thickness)	1/2
Wang et al. (2012)	Reinforced concrete slab	$1.25 \times 1.25 \times 0.05$ m (length \times width \times height)	1/1.67
Noam et al. (2014)	Circular clamped plates	0.05×0.005 m (radius \times thickness)	1/1.6
Kong et al. (2017)	Steel box structures	$0.6 \times 0.6 \times 0.6$ m (length \times width \times height)	1/2
Yao et al. (2017)	Cabin structures	$0.8 \times 0.4 \times 0.4$ m (length \times width \times height)	1/2
Fu et al. (2021)	Steel plates	$10 \times 10 \times 0.1$ m (length \times width \times thickness)	1/20
Ren et al., 2022	Armor steel plates	$1.5 \times 1.5 \times 0.0045$ m (length \times width \times thickness)	1/2
Yao et al. (2022)	Steel box structures	$1.53 \times 1.53 \times 0.63$ m (length \times width \times height)	1/1.5

for the scaling of failures of structures, particularly for tensile failures, which were more sensitive to the strain rate, relevant advances were rarely reported.

In contrast to a large number of studies on the scaling law of structures against air blasts, the literature on the scaling law of structures against underwater explosions is rather scarce. Particularly, for the scaling of dynamic responses and failures of concrete gravity dams undergoing underwater explosions, to the best of the authors' knowledge, still, no relevant research has been reported. This is mainly attributed to the high complexity of this subject. It can be expounded from the load and the structural response two aspects as follows.

- (1) Load. Compared to the air blast, the underwater explosion is much more complicated, comprising the shock wave and the bubble pulse, two major physical phenomena. The shock wave is the direct consequence of the compressibility of the water and is not dependent on gravity. Thus, the small-scale model tests in pools or water tanks with normal gravity have been proved effective in modeling the shock wave on the conditions of the Mach similitude. However, the bubble oscillation is a direct result of the competition between the pressures inside and outside the bubble. The pressure outside the bubble refers to the hydrodynamic water pressure that can change significantly with the water depth due to the gravity effect. In addition, the bubble motion upwards is affected by the buoyancy that also results from gravity. In this way, to simulate the bubble pulse, the gravity-related Froude similitude must be satisfied. The small-scale model tests in pools or water tanks with normal gravity fail to achieve this. Thereby, the small-scale model tests in a centrifuge with hyper-gravity are required, where the Mach and Froude similitudes can be satisfied simultaneously (Hu et al., 2017).
- (2) Structural response. The structural responses of concrete gravity dams are complicated. It can be expounded at the following three aspects.

Firstly, compared to the metal materials commonly adopted in previous studies (Neuberger et al., 2007; Noam et al., 2014; Yao et al., 2017; Fu et al., 2021), the concrete material is more complex. Controlled by the physical mechanisms due to the concurrence of microcracks and pores, the concrete material can exhibit very complicated mechanical behaviors, including compaction due to pore collapse, shear dilatation, pressure dependence, strain-rate dependence, Lode-angle dependence, strain hardening, strain softening, etc. Moreover, as a typical brittle material, the concrete material can fail easily in tension accompanied by the growth and coalescence of microcracks. In light of this, the relatively simpler metal materials were commonly adopted in previous studies (see Table 2), and only the study by Wang et al. (2012) has experimentally explored the scaling of dynamic responses and failures of reinforced concrete slabs.

Secondly, the gravitational forces can not be ignored for concrete gravity dams. As mentioned previously, the gravitational forces can not scale for scaled-down experiments conducted on the ground with normal gravity. However, the error brought was acceptable, since, in previous studies (Neuberger et al., 2007; Wang et al., 2012; Noam et al., 2014; Yao et al., 2017), the geometrical size of the structure prototype was very small (see Table 2) such that the gravitational forces were not significant and can be ignored compared to the high accelerations due to structural responses. However, for the concrete gravity dam concerned here, its geometrical size was noticeably larger, with the dam height possibly up to several hundred meters. Thus, the gravitational forces were significant. Actually, as the name indicated, the gravity effect was critical to a concrete gravity dam, which played a major role in the dam's stability. In addition, in previous studies with structures of small geometrical sizes, the geometrical scaling factor β can be large (generally larger than 1/10 as indicated in Table 2), such that the differences in gravitational forces of the model and the prototype were not

pronounced. However, considering the large geometrical size of concrete gravity dams, the geometrical scaling factor β must be sufficiently small (generally smaller than $1/50$) so that the experimental cost of each test was affordable, and thus systematic investigations with a series of parallel tests were possible. However, this will introduce great deviations into the gravity field of the dam model compared to the dam prototype. For these reasons, the small-scale model tests conducted on the ground with normal gravity were not suitable. Again, the small-scale centrifuge test in a centrifuge with hyper-gravity was the optimal choice since the centrifuge can effectively provide a similar gravity field like that for the dam prototype.

Thirdly, correcting the scaling law with consideration of the strain-rate effect for concrete gravity dams is challenging. As stated above, the corrected methods in previous studies (Mazzariol et al., 2016; Kong et al., 2017; Fu et al., 2021; Yao et al., 2022) were still far from our ambitions to scale the dynamic responses and failures of concrete gravity dams. To address this issue, the typical failure modes and the underlying failure mechanisms of concrete gravity dams due to underwater explosions needed to be well understood. However, currently, it is still a pending subject.

Restricted by these critical requirements, advances in the scaling law of concrete gravity dams subjected to underwater explosions were not reported yet. The purpose of this study is to narrow this gap through small-scale centrifuge tests and numerical simulations.

It should be noted that this study mainly concerns the near-field underwater explosion with the standoff distance generally smaller than the maximum bubble size. In this circumstance, both the peak pressure and the impulse of the shock wave are significantly higher than those of the bubble pulse (Huang et al., 2022a), and thus the dam will be destroyed by the shock wave before the bubble pulse arrives (Huang et al., 2020a, 2022a). Thereby, in this study, the focus will be paid to the scaling of dynamic responses and failures of concrete gravity dams due to the shock wave, while the effect of bubble pulse is neglected.

To scale the gravitational forces of concrete gravity dams, small-scale centrifuge tests are used to establish and validate the numerical model. Besides, to well predict the severe dam failures and scale them, a developed concrete constitutive model in hydrocode that is not relevant to the fracture mechanics or fracture toughness is employed. However, to propose a complete scaling law with consideration of the strain-rate effect for this complicated problem is challenging. In this study, the dimensional analysis-based scaling theory in Tables 1 and i.e., the geometrical scaling law for the dam structure and the Hopkinson scaling law for the shock wave, is employed. However, the strain-rate effect will be highlighted and based on this, the corrected scaling law with consideration of the strain-rate effect will be considered in the future.

The remainder of this paper is structured as follows. In Section 2, the research methods, including two small-scale centrifuge tests and numerical simulations, are introduced. In Section 3, the scaling of dam dynamic responses and failures are presented. The strain-rate effect is highlighted. In Section 4, several conclusive remarks are given. A mesh convergence study is presented in Appendix A. More results are given in Appendix B to consolidate the conclusions.

2. Methods

2.1. Centrifuge tests

Physical modelling of concrete gravity dams subjected to underwater explosions through small-scale centrifuge tests was highly desired. Recently, Huang et al. (2020a) carried out several small-scale centrifuge tests to uncover the dam destructions caused by underwater explosions. Two of them, as summarized in Table 3, were used in this study to establish and validate the numerical model. Detailed information about the centrifuge tests has been presented in previous research (Huang et al., 2020a, 2022a, 2022b), and thus, only a brief introduction was presented here.

Table 3

Scheme of centrifuge tests.

Test no.	n (g)	W (g)	H_w (m)	L (m)	R_c (m)
UE-01	80	2.2	0.6	0.1	0.02
UE-02	50	1.1	0.6	0.1	0.1

Note: n denotes centrifugal acceleration, g is acceleration of gravity, W is explosive weight, H_w is water depth, L is detonation depth, R_c is standoff distance.

Fig. 1 illustrates the small-scale centrifuge model. The dam structure was composed of three independent and identical dam blocks. The Young's modulus of the concrete dam was 20.1 GPa. The compressive and tensile strength, respectively, were 14.9 MPa and 1.46 MPa. The cylindrical electric detonator was used to represent the explosive. The precise TNT equivalent of one electric detonator was determined as 1.1 g (Huang et al., 2020a). Before detonation of the electric detonator, the entire model placed in a centrifuge was centrifugally accelerated to a target centrifugal acceleration denoted by ng . The target centrifugal acceleration was then maintained to the end of the test.

In centrifuge test UE-01, the model was scaled by a geometrical scaling factor $\beta = 1/80$ with a centrifugal acceleration of 80 g. Two electric detonators with a total TNT equivalent of about 2.2 g were used. Besides, the electric detonators were placed very close to the dam upstream face with a standoff distance R_c of only 0.02 m. Thus, the dam was severely destroyed. In centrifuge test UE-02, the model was scaled by a geometrical scaling factor $\beta = 1/50$ with a centrifugal acceleration of 50 g. Only one electric detonator was employed, and the standoff distance was increased to 0.1 m. For both tests, the water depth H_w was 0.6 m, and the detonation depth L was 0.1 m. It should be noted that the main focus of this study was relevant to centrifuge test UE-01 since the dam failures were much more severe with the more destructive underwater explosion condition of centrifuge test UE-01 (Huang et al., 2020a).

2.2. Numerical simulation

2.2.1. Finite element model

Based on the small-scale centrifuge tests, the finite element model was established (Fig. 2). The Coupled Lagrangian-Eulerian method was employed to handle this fully coupled water-air-explosive-dam system. This method was available in software LS-DYNA and has been proved effective in modeling the whole process of concrete gravity dams undergoing underwater explosions (Wang et al., 2020a; Huang et al., 2022a, 2022b). With this method, the dam and the aluminum container were constructed by the Lagrangian mesh, while the water, the air, and the explosive were established using the Eulerian mesh. Only half of the centrifuge test model was modeled considering its symmetries. Symmetric boundary conditions were then applied to the symmetric planes. The three dam blocks were separately modeled. To reproduce the restrictions from the aluminum container in the centrifuge tests, the aluminum container was also modeled in the numerical simulation. Water waves, then, can be reflected by the container. To simulate the centrifugal acceleration, the hyper-gravity was vertically added to the numerical model. The hyper-gravity was added before the explosion through the dynamic relaxation method available in LS-DYNA. The coordinate direction and the origin of coordinates were indicated (Fig. 2). Several points with coordinates that were monitored were marked. Fig. 2 also illustrates the mesh discretization of the finite element model with a geometrical scaling factor $\beta = 1/80$. The solid hexahedral element was employed.

To define the interactions of interfaces between the three concrete dam blocks, and those between dam blocks and the aluminum container, the frictional contact algorithm available in LS-DYNA was employed. The keyword "CONTACT_ERODING_SURFACE_TO_SURFACE" was used. The frictional coefficient was defined by,

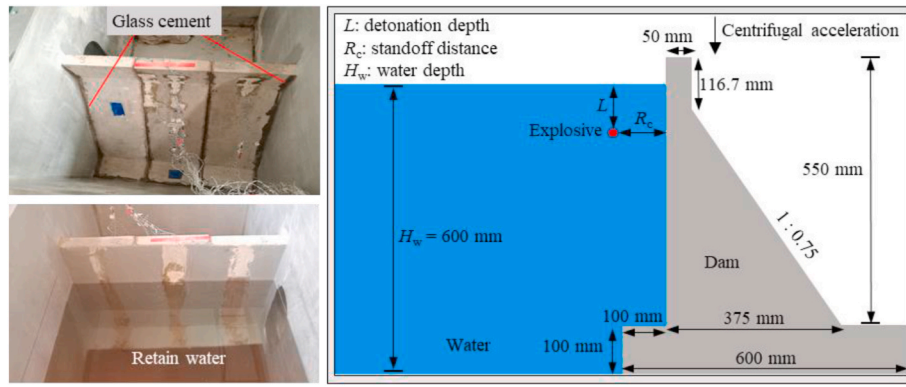


Fig. 1. Small-scale centrifuge test model of a concrete gravity dam subjected to an underwater explosion (Huang et al., 2022a).

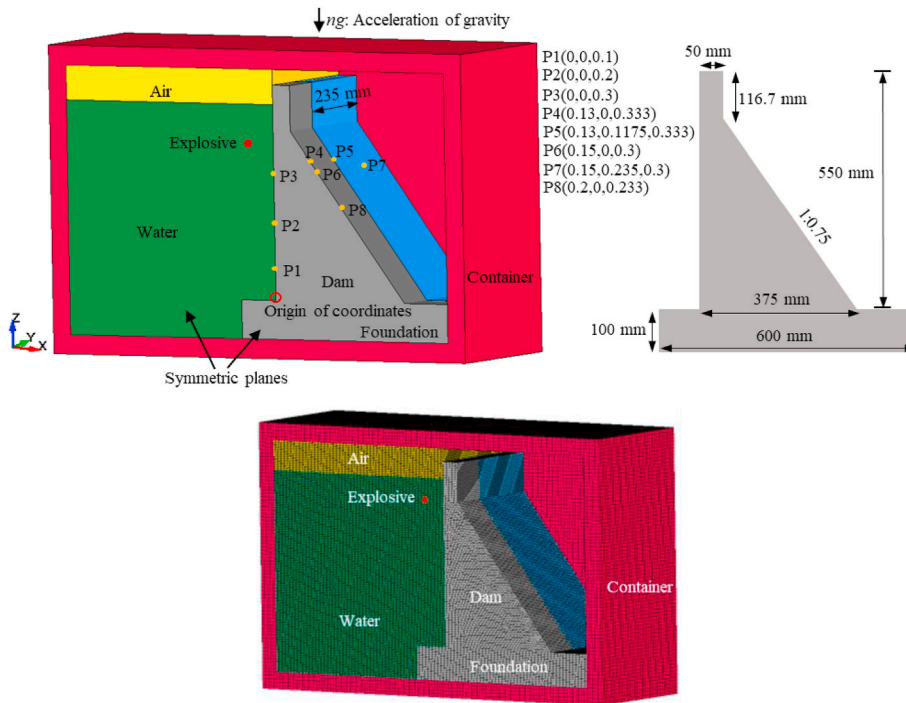


Fig. 2. Small-scale numerical model of a concrete gravity dam subjected to an underwater explosion (Huang et al., 2022b).

$$F_{\mu} = F_D + (F_S - F_D)e^{-\gamma V} \quad (2a)$$

where F_{μ} is the coefficient of friction, F_D is the dynamic coefficient of friction, F_S is the static coefficient of friction, and γ is the exponential decay coefficient. V is the relative velocity of the interface in contact, which is constantly updated during the numerical calculation. To evaluate the influence of friction on dam responses, pre-simulations with different frictional parameters (F_D , F_S , and γ) were carried out. Results demonstrated that the frictional parameters (F_D , F_S , and γ) owned very tiny influences. In this study, the frictional parameters $F_D = 0.05$, $F_S = 0.5$, and $\gamma = 0.07$, producing a frictional coefficient of about 0.5, for interactions between dam and dam as well as dam and container were employed.

It was noted that the numerical calculations were carried out in LS-DYAN. The time integration scheme and the time step determined by the main code of LS-DYNA were adopted. In LS-DYAN, the time step was dependent on the mesh size and can be controlled by the “CONTROL_TIMESTEP” keyword by introducing a scale factor. For blast loads, the default scale factor was 0.67 and was adopted in this study. For the numerical model with the geometrical scaling factor $\beta = 1/80$

with a mesh size of 6 mm, the time step determined by LS-DYAN was 1.84×10^{-6} s. The current and numerous numerical studies have proved that the time step determined by LS-DYNA was small enough to maintain stable calculations and produce convergent results.

To examine the scaling theory stated in Table 1, a numerical scheme, as presented in Table 4, was devised based on centrifuge test UE-01. Six finite element models were included with the geometrical scaling factors $\beta = 1, 1/10, 1/30, 1/50, 1/80,$ and $1/100$. Specifically, the numerical simulation SUE-05 was scheduled firstly in accordance with the centrifuge test UE-01, and then the other five numerical simulations were designed according to the scaling laws in Table 1. Based on the Hopkinson scaling law, the scaled distances for the six numerical simulations were maintained with a value of $0.154 \text{ m/kg}^{1/3}$. This parameter was quite small, with more than 1.1-ton TNT explosives detonated at a standoff distance of only 1.6 m for the dam prototype. Thus, severe dam destructions can be expected.

It should be noted that the scaling of dynamic responses and failures of concrete gravity dams against underwater explosions was conducted mostly based on the numerical scheme in Table 4. However, another numerical scheme also comprising six numerical simulations was

Table 4
Numerical scheme based on centrifuge test UE-01.

Parameters	Model					
	SUE-01	SUE-02	SUE-03	SUE-04	SUE-05	SUE-06
No.						
Scaling factor/ β	1	1/10	1/30	1/50	1/80	1/100
Acceleration of gravity/ ng	1	10	30	50	80	100
Dam height, h/m	44	4.4	1.47	0.88	0.55	0.44
Water depth, H_w/m	48	4.8	1.6	0.96	0.6	0.48
Standoff distance, R_c/m	1.6	0.16	0.053	0.032	0.02	0.016
Detonation depth, L/m	8	0.8	0.27	0.16	0.1	0.08
Explosive weight, W/kg	1126.4	1.1264	0.0417	9×10^{-3}	2.2×10^{-3}	1.1264
Scaled distance, $Z = R_c/W^{1/3}/m/kg^{1/3}$	0.154	0.154	0.153	0.154	0.154	0.154

scheduled (Table B1 in Appendix B), which was devised based on centrifuge test UE-02. This numerical scheme was of less interest since the scaled distance according to the Hopkinson scaling law was up to $0.9687 \text{ m/kg}^{1/3}$, and thus the dam failures were much slighter. Nevertheless, the scaling of dam failures based on this numerical scheme was also conducted and was presented in Appendix B. It was provided as a supplement to the numerical scheme in Table 4 to consolidate the conclusions.

Another issue that needs to be well considered is the mesh size effects of different models. Previous studies (Ferguson, 1995; Noam et al., 2014) suggested that the mesh size should be scaled by the geometrical scaling factor β with the mesh density kept. In this study, a mesh size of 6 mm was adopted for the small-scale model with $\beta = 1/80$ according to the mesh convergence study by Huang et al. (2022a). Then, the same mesh density was applied to the other five finite element models. However, to demonstrate that the mesh size will not affect the conclusions obtained, detailed mesh convergence studies for the prototype and small-scale models were presented in Appendix A.

2.2.2. Constitutive model for concrete

To well predict the highly non-linear dam responses against underwater explosion shock loadings is challenging. An advanced constitutive model in hydrocode should be employed considering the high pressure and high strain rate the dam encountered. In this study, the constitutive model developed by Huang et al. (2020b) was adopted. This model originated from the concrete model by Kong et al. (2018) by incorporating the free water effect (Rossi, 1991; Cadoni et al., 2001; Malecot et al., 2019). The free water effect was considered to account for the different mechanical behaviors between saturated concrete and dry concrete. This was critical since the dam structure served in the underwater environment, and thus, the concrete was actually saturated. A brief introduction of the Huang et al. model was presented below.

To define the deviatoric behaviour, two independent strength surfaces of the compressive meridian are employed, i.e.,

$$\sigma_m = \begin{cases} 3[P/(1-D_{\text{tot}}) + f_t^w] & P \leq 0 \\ 1.5(P + f_t^w)/\psi & 0 < P \leq f_c^w/3 \\ f_c^w + \frac{P - f_c^w/3}{a_1 + a_2 P} & f_c^w/3 < P \leq P_0 \\ w(2-w)\left(f_c^w + \frac{P_0 - f_c^w/3}{a_1 + a_2 P_0}\right) + (1-w)^2\left(f_c^w + \frac{P - f_c^w/3}{a_1 + a_2 P}\right) & P > P_0 \end{cases}, \quad (2b)$$

$$\sigma_r = \frac{P}{a_1 + a_2 P}, \quad (3)$$

where σ_m and σ_r are the maximum strength surface and the residual strength surface, respectively. P represents the hydrostatic pressure. D_{tot} is the total damage that will be defined later. w denotes the free water content of the concrete that is used to introduce the free water effect. In this study, the concrete dam is considered to be saturated, and thereby w equals to 1.0. f_c^w and f_t^w denote respectively the quasi-static compressive strength and tensile strength for the concrete with free water content w . ψ is ratio of the tensile meridian to the compressive meridian. a_1 and a_2 are parameters used to match with the triaxial compression test data. P_0 is a pressure threshold beyond which the capillary pores of the concrete are fully compacted. This value depends on the free water content. For saturated concrete concerned in this study, $P_0 = 130 \text{ MPa}$ is suggested.

Then the current failure surface $Y(\sigma_{ij})$ is defined by the interpolation based on the two strength surfaces and the total damage, i.e.,

$$Y(\sigma_{ij}) = r' [D_{\text{tot}}(\sigma_r - \sigma_m) + \sigma_m], \quad (4)$$

where r' denotes the ratio of the current meridian to the compressive meridian, used to account for the Lode-angle effect. The yield surface f is defined as,

$$f = \sqrt{3J_2} - Y(\sigma_{ij}), \quad (5)$$

where J_2 is the second deviatoric stress invariant.

To consider the strain-rate effect, the radial enhancement approach is adopted. With this approach, the current failure surface $Y(\sigma_{ij})$ is enhanced as,

$$Y = r_f Y(P/r_f), \quad (6)$$

where r_f denotes the dynamic increase factor (DIF) that is defined as ratio of the dynamic strength to the quasi-static strength. The DIF for concrete is defined as (Zhao and Wen, 2018),

$$\text{DIF}_t^w = g(\dot{\epsilon}, w) \cdot \text{DIF}_t, \quad (7)$$

$$\text{DIF}_c^w = (\text{DIF}_t^w - 1) \frac{f_t^w}{f_c^w} + 1, \quad (8)$$

where DIF_t^w and DIF_c^w respectively denote the DIF for tension and compression of concrete with free water content w . DIF_t represents the DIF for tension of dry concrete. $g(\dot{\epsilon}, w)$ is a function exceeding the unity that is introduced to account for the effect of free water on the strain-rate effect, which is defined as (Zhao and Wen, 2018),

$$g(\dot{\epsilon}, w) = \frac{\text{DIF}_t^w}{\text{DIF}_t} = \begin{cases} 1 & \dot{\epsilon} \leq 10^{-5} \\ -(1 + 0.15w)^{-\lg \dot{\epsilon} - 5} + 2 & \dot{\epsilon} > 10^{-5} \end{cases}, \quad (9)$$

where $\dot{\epsilon}$ is the strain rate. DIF_t for dry concrete required in Eqs. (6)–(8) is defined as (Xu and Wen, 2013),

$$\text{DIF}_t = \{[\tanh((\log(\dot{\epsilon}/\dot{\epsilon}_0) - W_x)S)](F_m/W_y - 1) + 1\} W_y, \quad (10)$$

with fitting constants $F_m = 10$, $W_x = 1.6$, $S = 0.8$, and $W_y = 5.5$. $\dot{\epsilon}_0 = 1 \text{ s}^{-1}$ represents the reference strain rate.

To define the damage model, a modified equivalent plastic strain λ is defined, i.e.,

$$\lambda = \begin{cases} \lambda_c = \sum \frac{\Delta \bar{\epsilon}_p}{d_1 (f_t^w/f_c^w + P/f_c^w)^{d_2}}, & P > 0 \\ \lambda_t = \sum \Delta \bar{\epsilon}_1, & P \leq 0 \end{cases}, \quad (11)$$

where λ_t and λ_c are the modified equivalent plastic strain for tension and compression, respectively. $\Delta \bar{\epsilon}_p$ is the effective plastic strain increment. $\Delta \bar{\epsilon}_1$ is the uniaxial plastic strain increment in tension. d_1 and d_2 are

damage parameters. Then, the tensile damage, D_t , is formulated as,

$$D_t = 1 - \left(1 + \left(c_1 \frac{\lambda_t}{\varepsilon_{\text{frac}}} \right)^3 \right) \exp \left(-c_2 \frac{\lambda_t}{\varepsilon_{\text{frac}}} \right) + \frac{\lambda_t}{\varepsilon_{\text{frac}}} (1 + c_1^3) \exp(-c_2), \quad (12)$$

where $\varepsilon_{\text{frac}}$ is the fracture strain. $c_1 = 3$ and $c_2 = 6.93$ are material constants. The compressive damage, D_c , is defined as,

$$D_c = \frac{\lambda_c}{\lambda_c + 1}. \quad (13)$$

Then, the total damage, D_{tot} , mentioned above is determined as,

$$D_{\text{tot}} = 1 - (1 - D_c)(1 - D_t). \quad (14)$$

For a constitutive model in hydrocode, a separated equation of state (EoS) is required to describe the material volumetric behavior. In the Huang et al. model, the EoS for wet concrete is proposed as,

$$P_{\text{tot}} = P_{\text{dry}} + bP_w, \quad (15)$$

where P_{tot} is the total pressure that contains two parts. One is contributed by the dry solid sketch, described by P_{dry} , and the other is by the free water, defined by P_w . b is a coefficient used to scale the contribution from the free water. $b = 0.5$ is suggested Huang et al. (2020c). P_{dry} is defined as (EoS #8 in commercial software LS-DYNA),

$$P_{\text{dry}} = C(\mu) + h_0\theta(\mu)E_0, \quad (16)$$

where μ is the volumetric strain. E_0 is the internal energy per unit initial volume. h_0 is the ratio of specific heat. $C(\mu)$ and $\theta(\mu)$ are the tabulated pressure and temperature as functions of the volumetric strain, respectively. The widely used EoS for water is used to define P_w , i.e.,

$$P_w = \frac{\rho_0 C^2 \bar{\mu} \left[1 + \left(1 - \frac{\gamma_0}{2} \right) \bar{\mu} - \frac{\alpha \bar{\mu}^2}{2} \right]}{\left[1 - (S_1 - 1) \bar{\mu} - S_2 \frac{\bar{\mu}^2}{\bar{\mu} + 1} - S_3 \frac{\bar{\mu}^3}{(\bar{\mu} + 1)^2} \right]} + (\gamma_0 + \alpha \bar{\mu})E, \quad (17)$$

where $\bar{\mu} = \mu - \mu_0$, and μ_0 is the volumetric strain corresponding to the consolidation pressure P_0 . The reduced volumetric strain $\bar{\mu}$ is introduced which means that the free water starts to act only when all the pores occupied by the air are consolidated. E is the internal energy per unit volume. C is the intercept of the particle velocity $v_s(v_p)$ curve. S_1 , S_2 , and S_3 are the coefficients of the slope of the $v_s(v_p)$ curve. ρ_0 is the initial density of water. γ_0 is the Grüneisen gamma. α is the first order volume correction to γ_0 . The values of these parameters for water are: $\rho_0 = 1000 \text{ kg/m}^3$, $C = 1480 \text{ m/s}$, $S_1 = 2.56$, $S_2 = 1.986$, $S_3 = 1.2268$, $\gamma_0 = 0.35$, $E = 1.89 \times 10^6 \text{ J/m}^3$, $V_0 = 1.0$, $\alpha = 0$.

With the finite element method, the element erosion criterion is critical which is used not only to trigger the initiation and growth of cracks but also to delete the distorted elements appeared in larger deformation problems. Kong et al. (2018) proposed two element erosion criteria, i.e., the equivalent strain-based element erosion criterion for compression and the damage-based element erosion criterion for tension. For compressive failures, elements are deleted when the equivalent compressive strain $\varepsilon_{\text{cp}} = \sum \Delta \bar{\varepsilon}_p$ is larger than a user-defined critical value ε_{cf} . Similarly, for tensile failures, elements are deleted when the tensile damage-based modified equivalent tensile strain λ_t is larger than a user-defined critical value λ_{tf} . These element erosion criteria have been examined that can be suitable for concrete structures against impact and blast loadings (Kong et al., 2018; Huang et al., 2020a) and thereby were adopted in the current study. The user-defined critical value $\varepsilon_{\text{cf}} = 0.5$ for compression and $\lambda_{\text{tf}} = 0.015$ for tension suggested by Kong et al. (2018) were used.

Except for the material constants that have been given above, all the material parameters required in the Huang et al. model for concrete are summarized in Table 5. The strengths and Young's modulus are acquired from the centrifuge tests. Other parameters are obtained by using the automatic parameters generation procedure available in the Huang et al. model.

Table 5
Parameters for the concrete.

Parameter	Value	Parameter	Value
Compressive strength (MPa)	15.2	Strength parameters a_2 (MPa ⁻¹)	0.25×10^{-3}
Tensile strength (MPa)	1.49	Damage parameters d_1	0.04
Elastic modulus (GPa)	20.1	Damage parameters d_2	1.5
Poisson's ratio	0.2	Fracture strain $\varepsilon_{\text{frac}}$	0.015
Free water content w	1.0	Coefficient b	0.5
Pressure threshold P_0 (MPa)	130	Parameters of EoS for dry concrete	(Refer to Kong et al. (2018))
Strength parameters a_1	0.5876		

To model the pressure of water, Eq. (17) will also be used and the reduced $\bar{\mu}$ in Eq. (17) should be replaced by μ . To model the pressure released by chemical energy during the explosion, the widely used Jones–Wilkins–Lee formula is adopted, which reads as,

$$P = A \left(1 - \frac{\omega}{R_1 V} \right) e^{-R_1 V} + B \left(1 - \frac{\omega}{R_2 V} \right) e^{-R_2 V} + \frac{\omega E_e}{V}, \quad (18)$$

where V denotes the relative volume of the detonation product. E_e is the internal energy per unit volume of explosive. A , B , R_1 , R_2 , ω are material parameters. For TNT explosive, the following widely used parameters are adopted. The density of the TNT explosive $\rho_e = 1600 \text{ kg/m}^3$, $A = 3.712 \times 10^{11} \text{ Pa}$, $B = 3.231 \times 10^9 \text{ Pa}$, $R_1 = 4.15$, $R_2 = 0.95$, $\omega = 0.3$, and $E_e = 7.0 \times 10^9 \text{ J/m}^3$.

2.2.3. Validation of numerical model

To obtain reliable conclusions, the numerical model must be adequately validated by comparisons with experimental results. In this study, the employed numerical model was established based on the small-scale centrifuge tests and was validated by comparisons with the centrifuge test results. The relevant information was reported in previous research (Huang et al., 2020a, 2022a, 2022b). Results demonstrated that the established numerical model was appropriate, and the numerical predictions under different underwater explosion scenarios can well accord with the corresponding centrifuge test results. Details can be found in the mentioned literature and were not repeated here.

3. Results

Based on the numerical scheme in Table 4, numerical calculations were carried out. Results were presented in this section. Dam dynamic responses including energy, velocity, displacement, strain, strain rate, and stress were collected, and the scaling of them was conducted according to the scaling theory in Table 1. Similarities of dam failures between the prototype and small-scale models were discussed. The strain-rate effect on the scaling of dam dynamic responses and failures were highlighted.

3.1. Scaling of dam dynamic responses

3.1.1. Shock wave pressure

The similarity of underwater explosion shock loading is the basis of the proper scaling of dam dynamic responses. According to the Hopkinson scaling law, self-similar blast waves will be generated with explosives detonated at an identical scaled distance $Z = R_c/W^{1/3}$. In light of this, the six numerical simulations, as presented in Table 4, are designed with an identical scaled distance $Z = 0.154 \text{ m/kg}^{1/3}$. Fig. 3 depicts the shock wave pressure histories of points P2 and P3 (see Fig. 2). For visual clarity, results of representative models with scaling factors $\beta = 1, 1/30$, and $1/100$ are plotted and compared with the scaled time t/β . It can be found that the shock wave pressure histories for models with different

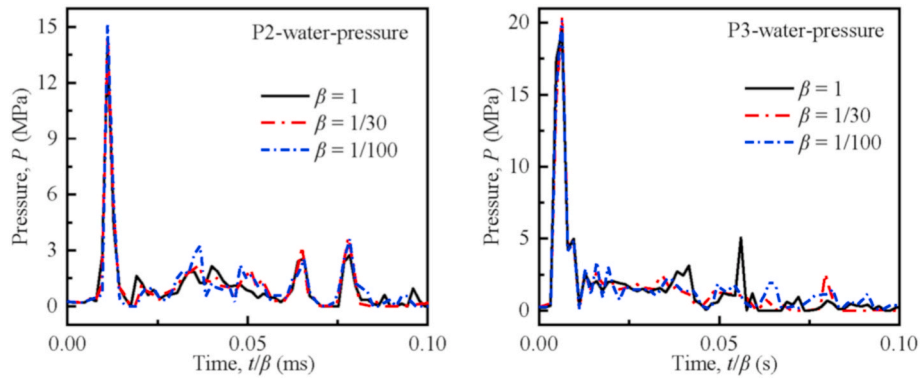


Fig. 3. Shock wave pressure histories of points P2 and P3.

scaling factors merge virtually into one single curve. This indicates that by maintaining the scaled distance, the numerically predicted shock wave pressures are similar and thus can follow the Hopkinson scaling law. Since the validity of the Hopkinson scaling law in scaling of blast effects has been widely verified for both air blasts (Neuberger et al., 2007) and underwater explosion shock loadings (Hu et al., 2017), more validation results are not repeated here.

3.1.2. Energy

The investigated problem involves a coupled system that comprises water, explosives, air, dam structures, and an aluminum container. Once the explosive is detonated, the explosive energy will be absorbed by other components in this system. The energy of the middle dam block that is very close to the explosion is concerned. There are two different energy forms in the dam, i.e., the absorbed internal energy and the kinetic energy due to movement. According to the scaling theory (Table 1), the energy Q is scaled by β^3 , based on which the explosive weight (relevant to the explosive energy) is scaled as shown in Table 4. Thus, basically, if the coupled systems scaled by different scaling factors are similar, the dam energy should also obey the scaling law.

Fig. 4 compares the normalized time-energy curves of dam models with different scaling factors. The energy is normalized as Q/β^3 , and the time is t/β . In general, for both internal energy and kinetic energy of the dam, the normalized time-energy curves with different scaling factors are comparable. Further, the peak values of dam internal energy and dam kinetic energy are collected and plotted in Fig. 5. Before normalization, the dam peak internal energy and kinetic energy fall on two separate curves but show a similar decreasing tendency with an increase of $1/\beta$ (Fig. 5(a)). However, after normalization to obtain the energy ratios Q^M/Q^P (superscript M represents the model and superscript P represents the prototype, likewise hereinafter), the dam peak internal

energy and kinetic energy fall almost on one single curve that can be well predicted by the scaling law (Fig. 5(b)). These observations indicate that the energy of the dam obeys the scaling law in Table 1. This is critical since it makes the scaling of the more complex dam dynamic responses and failures possible.

3.1.3. Velocity

Results above demonstrate that the dam kinetic energy can well accord with the scaling law, i.e., $Q^M/Q^P = \beta^3$. The kinetic energy Q depends on the mass W and the velocity v . With identical material density and geometrically similar models, the scaling of the mass can be guaranteed, i.e., $W^M/W^P = \beta^3$. This implies that the velocity can also obey the scaling law, namely, the velocities of the prototype and models are identical.

To verify this, Fig. 6 compares the velocity histories of some points of the dam models with $\beta = 1, 1/30$, and $1/100$. It is noted that the x-velocity in the figures represents velocity in the x-direction, and the z-velocity denotes velocity in the z-direction, and likewise for those below for displacement, strain, and stress. The coordinate direction and positions of referred points have been marked in Fig. 2. It can be found that for different points, the time-velocity curves of models with different scaling factors merge almost perfectly into one single curve. In addition, by collecting the peak velocities of more points, it is found that the peak velocities are not influenced by the scaling factor (Fig. 7(a)). Further, by normalization, the velocity ratios v^M/v^P are summarized and plotted in Fig. 7(b). It is found that for different scaling factors and different points, the velocity ratios v^M/v^P approximate the unity, suggesting that the velocities of the prototype and models are close. This finding indicates that dam velocity responses obey the scaling law in Table 1.

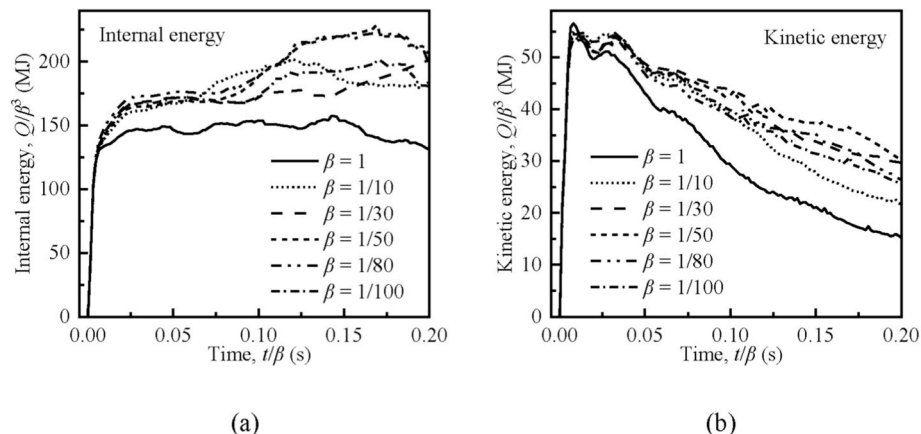


Fig. 4. Normalized time-energy curves: (a) dam internal energy and (b) dam kinetic energy.

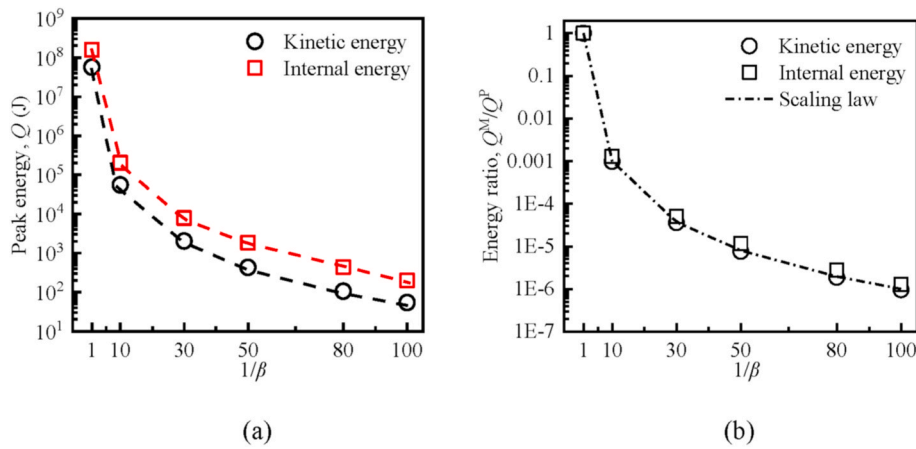


Fig. 5. Peak energy of the middle dam block: (a) Q - $1/\beta$ curve and (b) Q^M/Q^P - $1/\beta$ curve.

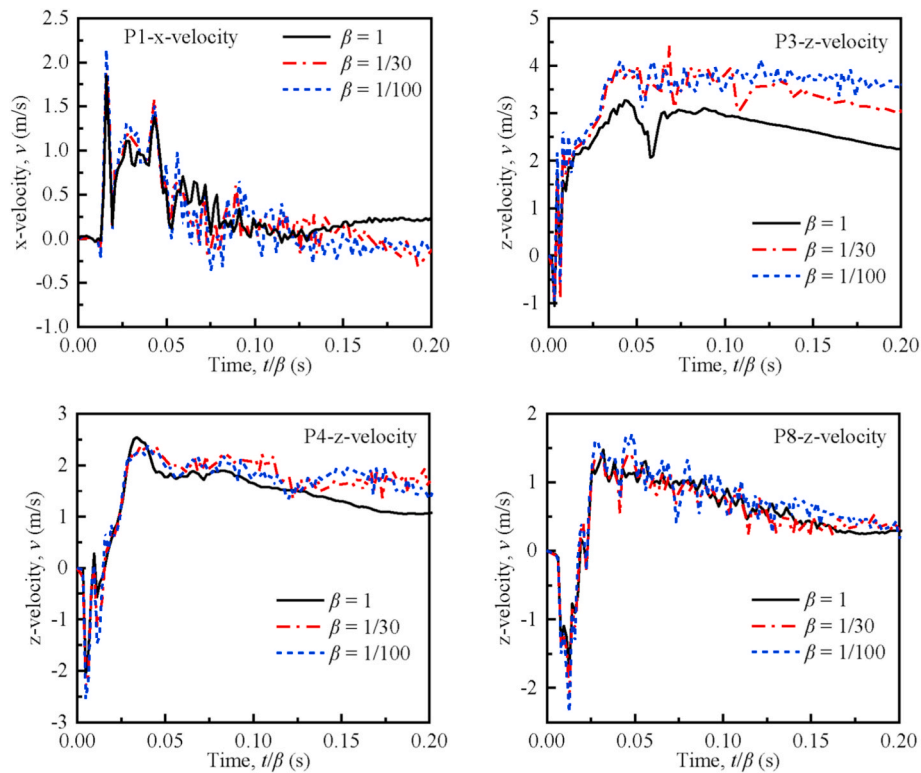


Fig. 6. Time-velocity curves.

3.1.4. Displacement

The good scaling of dam velocity responses implies that the dam displacement responses can also be well scaled. Fig. 8 illustrates the normalized time-displacement curves of some points of the dam models. Based on the scaling law (Table 1), the displacement is normalized as δ/β , and the time is t/β . It can be viewed that the normalized time-displacement curves with different scaling factors are generally comparable. In addition, by collecting the peak displacements, it is found that the peak displacements of different points fall on separate curves, but all exhibit a similar decreasing tendency with an increase of $1/\beta$ (Fig. 9(a)). Then, by summarizing the displacement ratios δ^M/δ^P , it is found that for different scaling factors and different points, the displacement ratios δ^M/δ^P fall almost on one single curve that well agrees with the predictions by the scaling law (Fig. 9(b)). These observations suggest that the dam displacement responses can comply with the scaling law in Table 1.

3.1.5. Strain

The strain is well-known to be associated with displacement (deformation). Roughly speaking, the strain ϵ of an element can be defined as the relative deformation Δl normalized by the original element length l_0 , i.e., $\epsilon = \Delta l/l_0$. More mathematically, the strain tensor ϵ is determined by the symmetrical form of the deformation (displacement) gradient tensor F , i.e., $\epsilon = (F + F^T)/2$. The dam displacement responses are demonstrated to be well scaled, thus, the scaling of strain can be expected. To confirm, Fig. 10 depicts the time-strain curves of some points of the dam models. In general, the strain histories with different scaling factors are comparable. The whole tendency is similar, while the peak strains display some deviations. Table 6 summarizes more peak strains. It is noted that strains marked with the symbol “-” represent compression and “+” represent tension. It is found that the peak x-strains of dam models with different scaling factors are close with an average error (absolute value) to the prototype as low as 12.7% and a

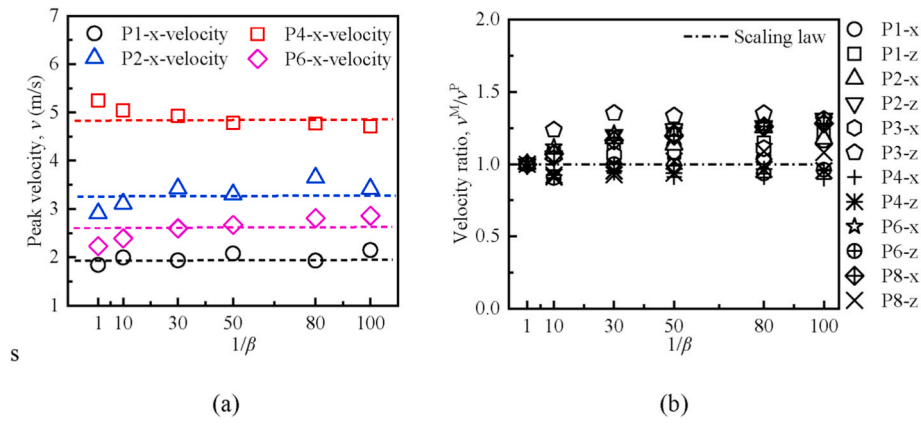


Fig. 7. Peak velocities of some points of the dam: (a) v - $1/\beta$ curve and (b) v^M/v^P - $1/\beta$ curve.

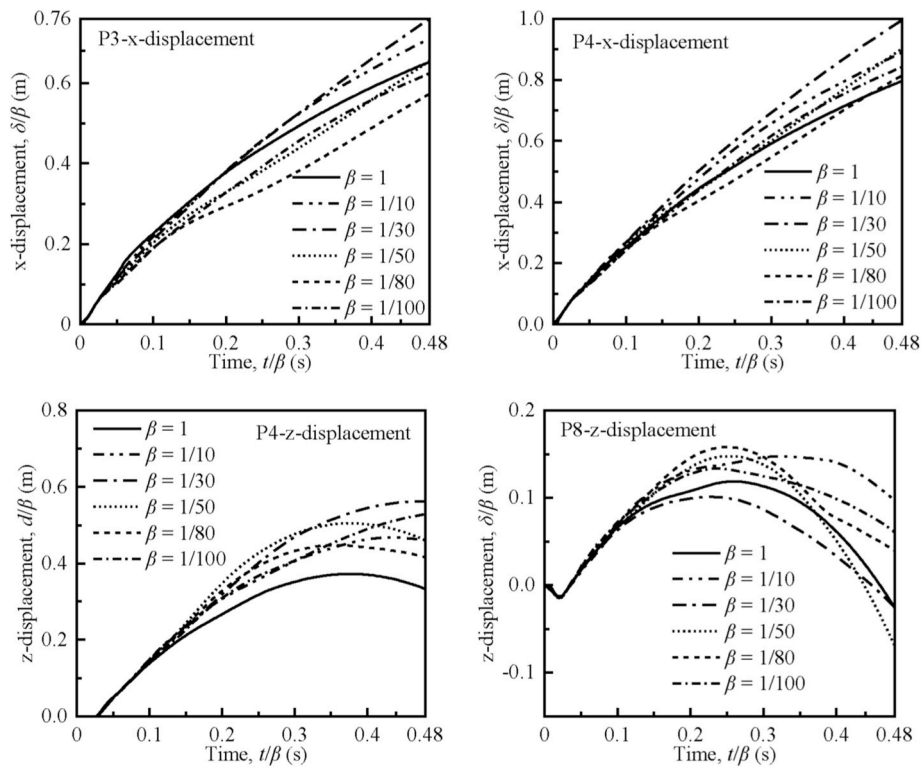


Fig. 8. Normalized time-displacement curves.

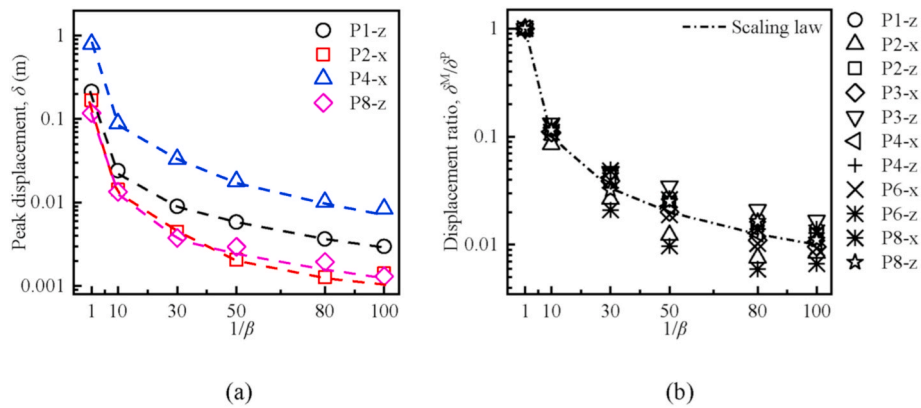


Fig. 9. Peak displacements of some points of the dam: (a) δ - $1/\beta$ curve and (b) δ^M/δ^P - $1/\beta$ curve.

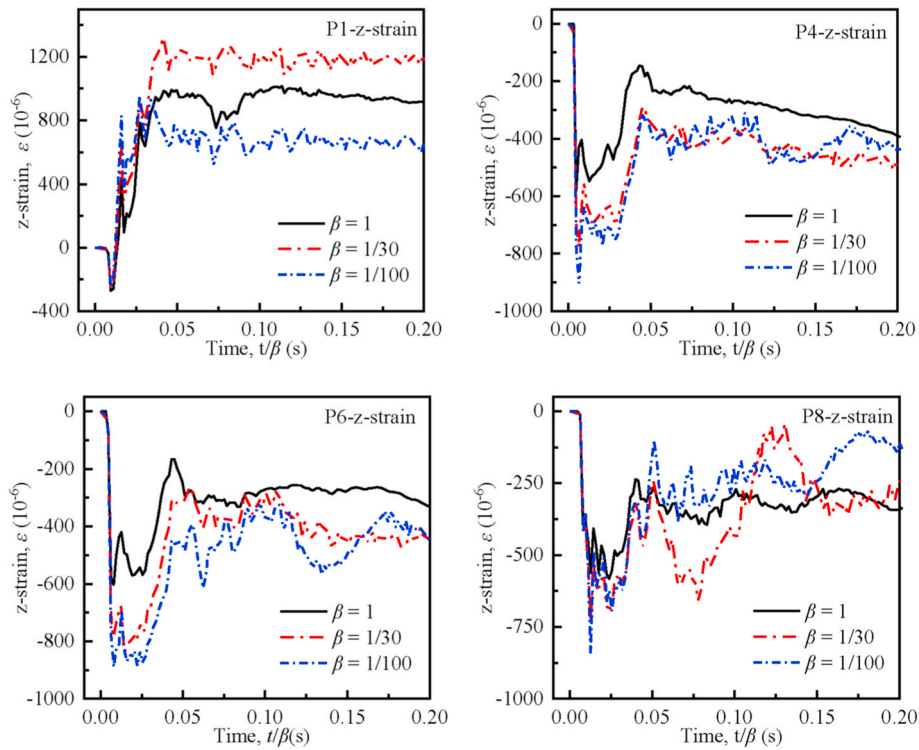


Fig. 10. Time-strain curves.

Table 6
Summary of peak strain.

Peak strain (10^{-6})	$\beta = 1$	$\beta = 1/10$	$\beta = 1/30$	$\beta = 1/50$	$\beta = 1/80$	$\beta = 1/100$
P1, x-	-420	-435 (+3.6%)	-494 (+17.6%)	-510 (+21.4%)	-507 (+20.7%)	-552 (+31.4%)
P2, x-	-862	-867 (+0.6%)	-853 (-10%)	-861 (-0.1%)	-754 (+12.5%)	-856 (-0.7%)
P3, x-	-1830	-1840 (+0.5%)	-1770 (-3.3%)	-1740 (-4.9%)	-1970 (+7.7%)	-1690 (-7.7%)
P4, x-	-285	-320 (+12.3%)	-339 (+18.9%)	-347 (+21.8%)	-348 (+22.1%)	-357 (+25.3%)
P8, x-	-146	-152 (+4.1%)	-180 (+23.3%)	-188 (+28.8%)	-155 (+6.2%)	-163 (+11.6%)
P1, z+	948	1200 (+26.6%)	1170 (+23.4%)	907 (-4.3%)	791 (-16.6%)	665 (-29.9%)
P2, z+	6150	5600 (-8.9%)	3450 (-43.9%)	2510 (-59.2%)	1860 (-69.8%)	1460 (-76.3%)
P3, z+	5270	6000 (+13.9%)	2890 (-45.2%)	1910 (-63.8%)	2710 (-48.6%)	2110 (-60%)
P4, z-	-583	-664 (+13.9%)	-780 (+33.8%)	-842 (+44.4%)	-882 (+51.3%)	-915 (+56.9%)
P6, z-	-603	-710 (+17.7%)	-786 (+30.3%)	-821 (+36.2%)	-850 (+41.0%)	-889 (+47.4%)
P8, z-	-562	-644 (+14.6%)	-727 (+29.4%)	-774 (+37.7%)	-828 (+47.3%)	-842 (+49.8%)

Note: strain marked with symbol ‘-’ represents compression and ‘+’ represents tension.

maximum error of 31.4%. However, for the peak z-strains, the average error increases to 38.1%, and the maximum error is even up to 76.3%. This observation suggests that the dam strain responses in the x-direction and z-direction show different scalabilities. This difference mainly arises from the different failure modes of the dam in the two directions.

According to the previous studies (Huang et al., 2020a, 2022a, 2022b), dam responses in the x-direction mainly belong to the dam local responses, which are caused by the direct impact of the shock wave. These local responses manifest themselves mainly as crush failures and thus are generally dependent on the dam compressive behaviors. However, dam responses in the z-direction mainly belong to the dam structural responses, which are controlled by the structural bending-induced tensile failure mode. More specifically, the shock loadings upstream act as bending loads and force the dam to bend downstream. In this way, the dam upstream face in the z-direction is under tension (see Points P1, P2, and P3 in Table 6) and can be damaged due to tensile failures, while the dam downstream face in the z-direction is accordingly under compression (see Points P4, P6, and P8 in Table 6). Clearly, the dam local responses in the x-direction such as crush failures are more straightforward, mainly depending on the shock wave peak

pressures. By contrast, the dam structural responses in the z-direction are complicated, involving not only the shock wave peak pressure but also its impulse. With identical scaled distance designed by the Hopkinson scaling law, the shock wave peak pressures are close (Fig. 3), however, their impulses are dissimilar. This accounts for the different scalabilities of dam strain responses in the x-direction and z-direction.

Fig. 11 summarizes the strain ratios ϵ^M/ϵ^P of different points. Compared to the good scaling of dam velocity and displacement responses (Figs. 7 and 9), the dam strain responses exhibit deviations, and the error increases with an increase of $1/\beta$. Nevertheless, considering the high complexity of this problem and the average error of only 26.6% for all peak strains in Table 6, the dam strain responses are generally considered to follow the scaling law.

3.1.6. Strain rate

With strains being close, the strain rates of dam models will be $1/\beta$ times enhanced. Fig. 12 presents the strain-rate histories of two points before normalization. It is found that the peak strain rate of the prototype (point P2) is about 0.6 s^{-1} , and this value is about 18 s^{-1} for the model with $\beta = 1/30$, and 60 s^{-1} for the model with $\beta = 1/100$. In other

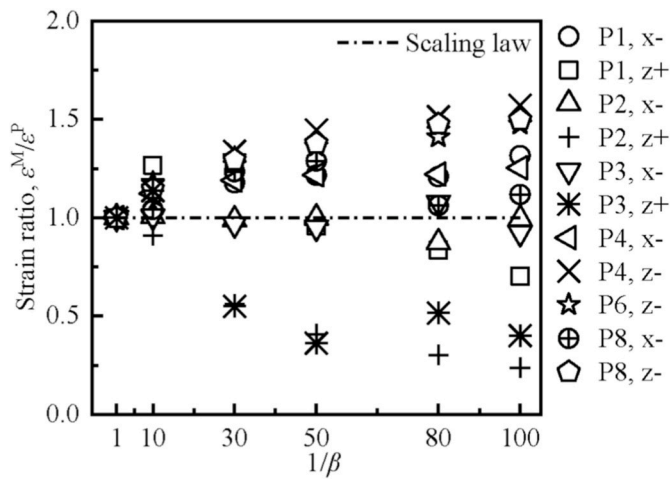


Fig. 11. Strain ratios ϵ^M/ϵ^P versus $1/\beta$. (Note: strain marked with symbol ‘-’ represents compression and ‘+’ represents tension).

words, the strain rate of the geometrically similar small-scale model is enhanced and is about $1/\beta$ times that of the prototype. Further, with the strain rate $\dot{\epsilon}$ according to the scaling law being normalized to $\dot{\epsilon}/\beta$, it is observed that the normalized strain-rate histories (Fig. 13) merge almost into one single curve. By collecting more peak strain rates, it is viewed that the peak strain rates of different points fall into different curves but all show a similar increasing tendency as the factor $1/\beta$ increases (Fig. 14(a)). However, by normalization to summarize the strain rate ratios $\dot{\epsilon}^M/\dot{\epsilon}^P$, it is found that the strain rate ratios of different points fall into almost one single curve that can well comply with the scaling law (Fig. 14(b)). All these observations indicate that the strain rate obeys the scaling law and will be $1/\beta$ times enhanced in the small-scale models.

Fig. 15(a) and (b) depict respectively the peak DIF_t^w (dynamic increase factor for tension of saturated concrete) and DIF_c^w (dynamic increase factor for compression of saturated concrete) of some points varying with the scaling factor. As expected, for all points, both DIF_t^w

and DIF_c^w increase with an increase of $1/\beta$ due to the enhanced strain rates of models. This causes the materials of small-scale models to be strengthened, which is well-known as the non-scalability of the strain-rate effect. As a result, this may introduce errors in the scaling of dam dynamic stresses and failures.

3.1.7. Stress

Stress is a much more complicated variable that can be influenced by different involved mechanical behaviors of concrete, such as the strain-hardening behavior, the strain-softening behavior, and the strain-rate effect. Mathematically, the dynamic stress σ_d can be viewed as functions of the strain ϵ , the strain-hardening parameter (internal variable) k , the strain-softening parameter (damage) D , and the strain rate $\dot{\epsilon}$, i.e., $\sigma_d = f(\epsilon, k, D, \dot{\epsilon})$. In view of this, whether the stress can comply with the scaling law deserves more attention. Fig. 16 presents the time-stress curves of some points of the dam models with different scaling factors. In general, the stress histories with three different scaling factors are comparable, with the whole tendency being almost identical. For the peak stresses, it is observed that the negative (compressive) peak stresses with different scaling factors are close, but those positive (tensile) peak stresses show great deviations. Table 7 collects more peak stresses. The stress marked with the symbol ‘-’ represents compression and ‘+’ represents tension. It is found that for compressive peak stresses, the average error (absolute value) to the prototype is only 18.5%, and the maximum error is 54%. However, for tensile peak stresses, the average error increases to 325%, and the maximum error is even up to 691%. These findings imply that the compressive stress generally follows the scaling law, while the tensile stress seems not.

To interpret, remember the function, $\sigma_d = f(\epsilon, k, D, \dot{\epsilon})$. It must be noted that the employed Huang et al. model (Huang et al., 2020b) has currently not considered the strain-hardening behavior. Besides, the strain-softening behavior can influence the stress in the post-peak stage, however, it has no influence on the peak stress. In addition, the strain has been demonstrated in Section 3.1.5 that can be scaled. Thus, only the strain-rate effect is involved. In other words, the strain-rate effect should be responsible for the different scalabilities of dam compressive peak stresses and tensile peak stresses. It can be expected since, on one hand,

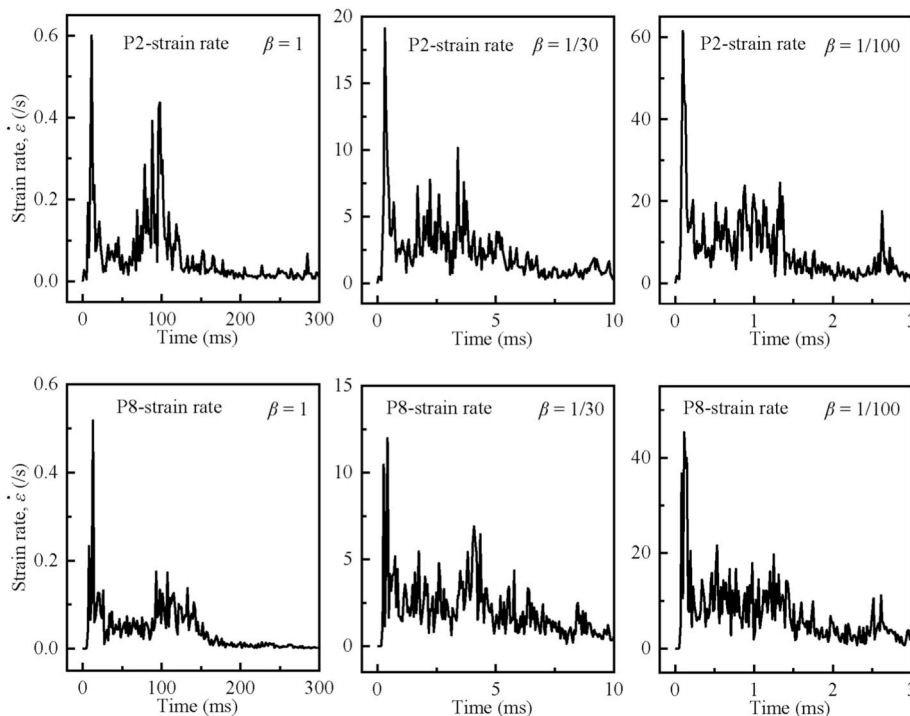


Fig. 12. Time-strain rate curves.

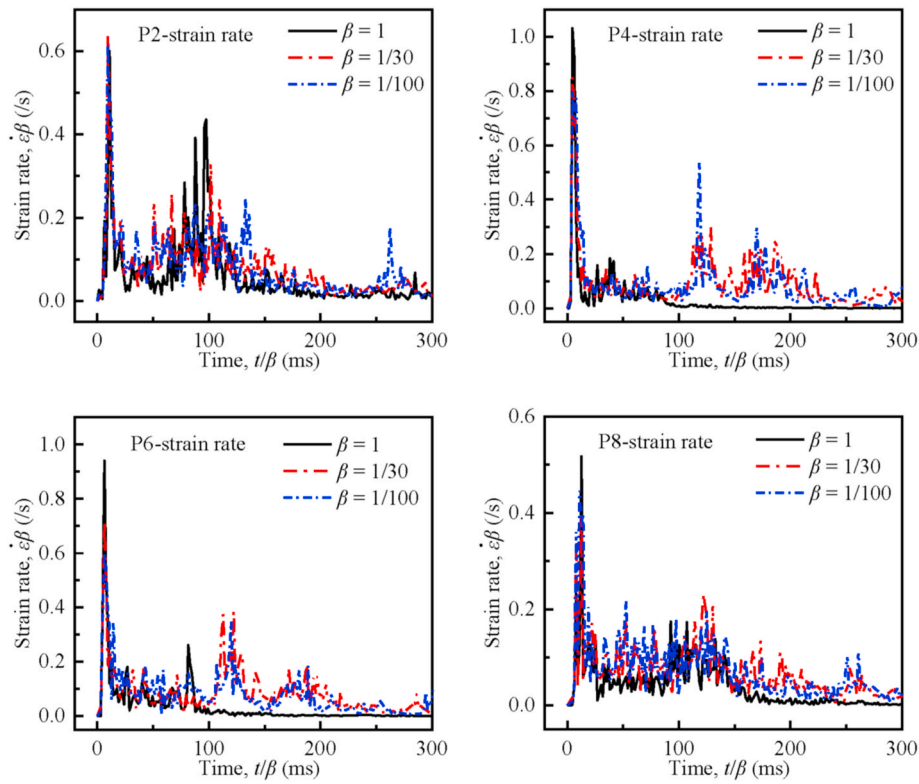


Fig. 13. Normalized time-strain rate curves.

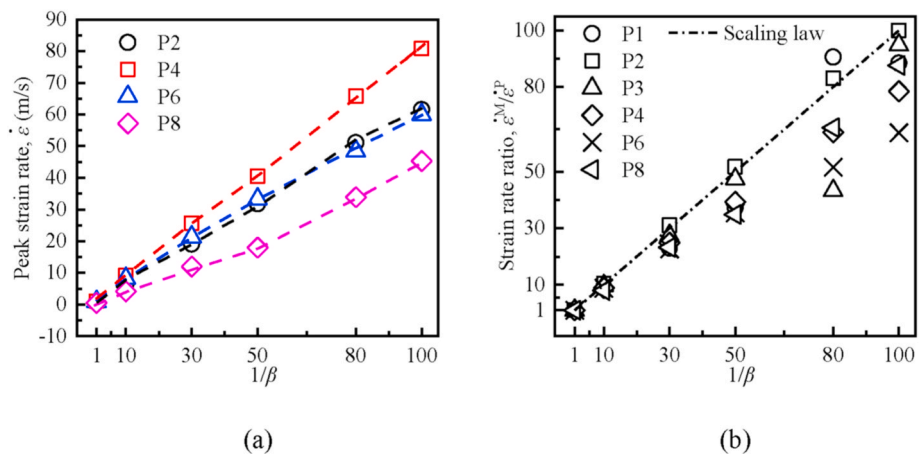


Fig. 14. Peak strain rates of some points of the dam: (a) $\dot{\epsilon}-1/\beta$ curve and (b) $\dot{\epsilon}^M/\dot{\epsilon}^P-1/\beta$ curve.

the strain rates of small-scale models are $1/\beta$ times enhanced (Figs. 13 and 14). Consequently, the error of peak stresses to the prototype generally increases as the scaling factor decreases (Table 7). On the other hand, the tensile stress is very sensitive to the strain rate with the DIF_t^w being increased from about 2 to 10 for the prototype and the model with $\beta = 1/100$, respectively (Fig. 15(a)). However, the compressive stress is of less strain-rate sensitivity, with the DIF_c^w for the prototype and the model with $\beta = 1/100$ being about 1.5 and 1.8, respectively (Fig. 15 (b)). Thereby, the dissimilar scalabilities of dam compressive stress and tensile stress are mainly attributed to the strain-rate effect.

Fig. 17 summarizes the compressive stress ratios σ^M/σ^P . It is found that for different points and different scaling factors, the compressive stress ratios are generally close to the unity, suggesting again that the dam compressive stress responses obey the scaling law.

4. Summary

Dam dynamic responses of different types are summarized in Figs. 18 and 19. Fig. 18 collects the ratios of dam model responses to dam prototype responses, whilst Fig. 19 gathers these ratios again with the dam model responses being converted to the dam prototype according to the scaling law in Table 1. It is found that before conversion, dam dynamic responses including energy, velocity, displacement, strain, and compressive stress fall into different curves, but all can well accord with the scaling law (Fig. 18); after conversion, all the converted dam dynamic responses are comparable with the ratios of converted dam model responses to the dam prototype responses approaching the unity (Fig. 19). These findings reveal that most of the dam dynamic responses can generally comply with the scaling law in Table 1.

It should be noted that the small-scale model is strengthened due to

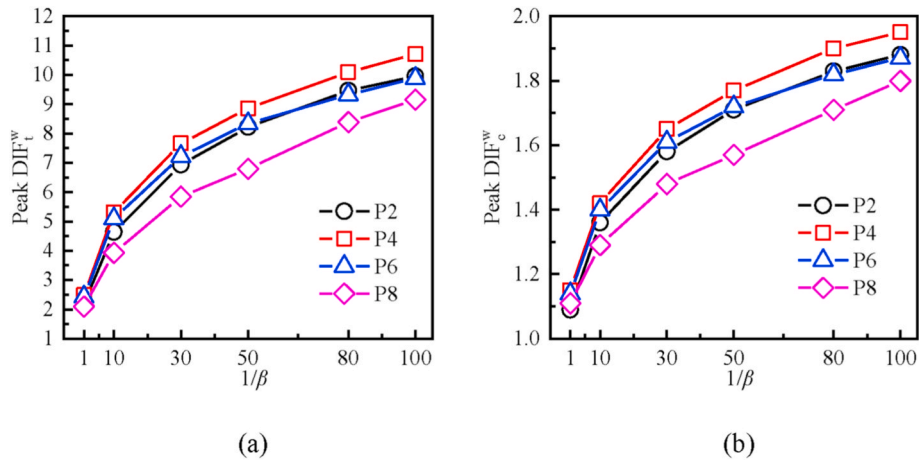


Fig. 15. Peak DIFs of some points of the dam: (a) DIF_t^w-1/β curve and (b) DIF_c^w-1/β curve.

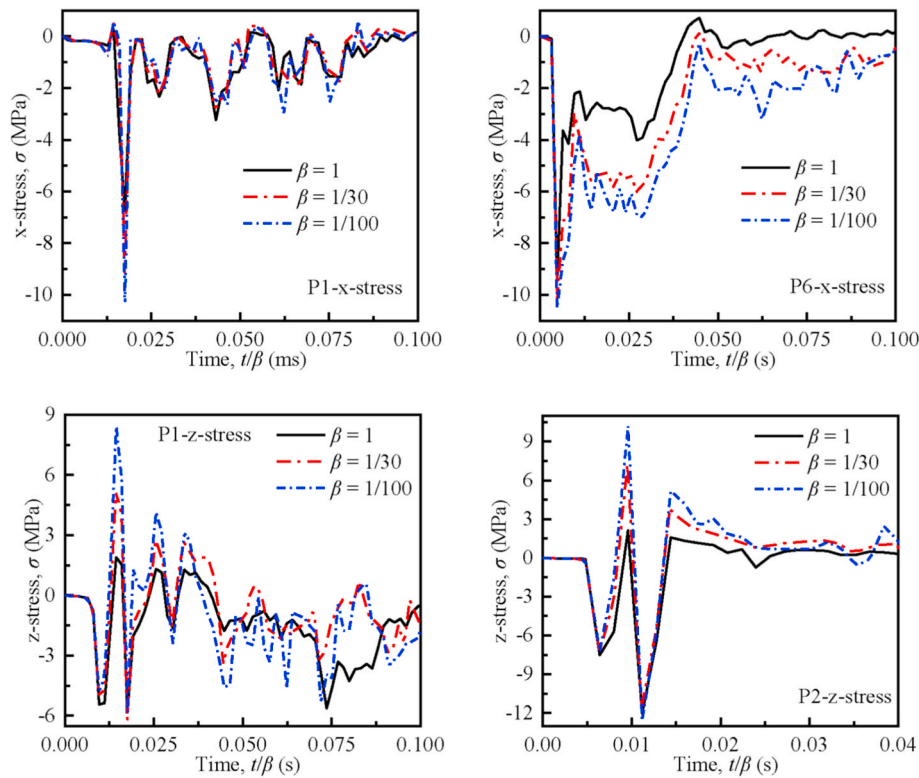


Fig. 16. Time-stress curves.

the enhanced strain rate. This, then, results in the differences in the dynamic responses of the prototype and small-scale models. For compressive stresses which are not very sensitive to the strain rate, the scaling theory in Table 1 still works. However, when the strain-rate effect is pronounced, such as in dam tensile stresses where the DIF_t^w can increase greatly, the scaling law is violated. Thus, more efforts are required to correct the dimensional analysis-based scaling law.

4.1. Similarity of dam failures

Fig. 20 and Fig. 21 illustrate the failure patterns of dam models with different scaling factors from the upstream and downstream perspectives, respectively. By inspections of Figs. 20 and 21, the following major observations can be found: (1) for all dams, the whole dam upstream face is covered by tensile damage, while almost no tensile damage

appears in the dam downstream face; (2) for all dams, the dam upper part with thin cross-section is severely destroyed and the failures are very similar with a horizontal fracture visible along the change of dam downstream slope; (3) for dams with $\beta = 1/30, 1/50, 1/80,$ and $1/100$, the failure patterns are almost identical and failures concentrate mainly on two areas, one for the dam upper part with a horizontal fracture, and the other for the dam body with a slant penetrating fracture; (4) for the dam with $\beta = 1/10$, the failure pattern is still quite similar to those with smaller scaling factors, with the slant penetrating fracture still visible in the dam body, however, an additional crack appears near the dam bottom; (5) for the dam prototype, the slant penetrating fracture in the dam body still holds, however, compared to the dam models, the dam prototype is the most severely destroyed with the appearance of much more cracks in the dam body.

To explain, it should be noted that the concrete gravity dam with an

Table 7
Summary of peak stress.

Peak stress (MPa)	$\beta = 1$	$\beta = 1/10$	$\beta = 1/30$	$\beta = 1/50$	$\beta = 1/80$	$\beta = 1/100$
P1, x-	-6.74	-7.64 (+13%)	-9.17 (+36%)	-9.53 (+41%)	-9.25 (+37%)	-10.4 (+54%)
P2, x-	-14.9	-15.9 (+6.7%)	-16.1 (+8.1%)	-16.7 (+12.1%)	-14.1 (-5.4%)	-17.0 (+14.1%)
P3, x-	-21.0	-22.4 (+6.7%)	-23.8 (+13.3%)	-23.4 (+11.4%)	-24.0 (+14.3%)	-23.5 (+11.9%)
P4, x-	-9.34	-10.0 (+7.1%)	-10.2 (+9.2%)	-10.4 (+11.3%)	-10.3 (+10.3%)	-10.5 (+12.4%)
P6, x-	-7.79	-8.34 (+7.1%)	-8.67 (+11.3%)	-9.11 (+16.9%)	-10.2 (+30.9%)	-10.4 (+33.5%)
P8, x-	-7.28	-8.26 (+13.5%)	-9.3 (+27.7%)	-9.82 (+34.9%)	-10.4 (+42.9%)	-10.4 (+42.9%)
P1, z-	-5.43	-5.18 (-4.6%)	-5.14 (-5.3%)	-4.95 (-8.8%)	-5.09 (-6.3%)	-4.89 (-9.9%)
P2, z-	-12.0	-11.9 (-0.8%)	-11.6 (-3.3%)	-12.3 (+2.5%)	-11.0 (-8.3%)	-12.6 (+5.0%)
P3, z-	-36.6	-38.1 (+4.1%)	-42 (+14.8%)	-38.9 (+6.3%)	-42.0 (+14.8%)	-39.1 (+6.8%)
P4, z-	-13.3	-14.9 (+12.0%)	-15.9 (+19.5%)	-16.4 (+23.3%)	-16.6 (+24.8%)	-17.0 (+27.8%)
P6, z-	-12.5	-14.2 (+13.6%)	-15.3 (+22.4%)	-15.8 (+26.4%)	-16.1 (+28.8%)	-16.8 (+34.4%)
P8, z-	-12.0	-13.8 (+15.0%)	-15.6 (+30.0%)	-16.5 (+37.5%)	-17.6 (+46.7%)	-17.7 (+47.5%)
P1, z+	1.90	3.28 (+72.6%)	5.19 (+173%)	6.41 (+237%)	7.73 (+307%)	8.43 (+344%)
P2, z+	2.13	4.74 (+123%)	7.22 (+239%)	8.36 (+293%)	9.70 (+355%)	10.19 (+378%)
P3, z+	1.52	3.71 (+144%)	8.13 (+435%)	8.56 (+463%)	12.02 (+691%)	10.96 (+621%)

Note: stress marked with symbol ‘-’ represents compression and ‘+’ represents tension.

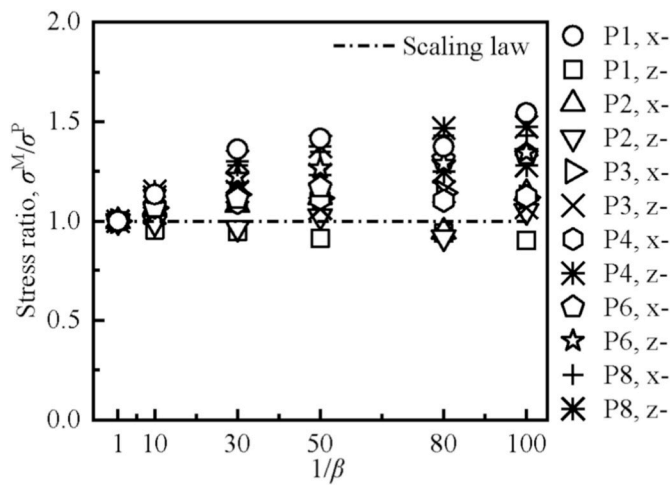


Fig. 17. Compressive stress ratios σ^M/σ^P versus $1/\beta$. (Note: stress marked with symbol ‘-’ represents compression).

approximately fixed bottom is like a vertical cantilever structure. The underwater explosion shock loadings upstream then act as bending loads that force the dam to bend downstream (Huang et al., 2020a, 2022a, 2022b). This can be reflected in the x-displacement field presented in Fig. 22. The legend is set to accord with the scaling law. Despite some deviations, all the dams are observed to bend downstream like vertical cantilever structures, with the x-displacement increasing from the dam top to the dam bottom. Then, the bending of the dam requires that the whole dam upstream face in the z-direction is under tension, and accordingly, the dam downstream face is under compression. This can be fully supported by the z-strain field given in Fig. 23. It is observed that for all dams, the z-strain field in the dam upstream face is positive (tension), whilst that in the dam downstream face is negative (compression). This explains why the whole dam upstream face is covered by tensile damage (Fig. 20), while almost no tensile damage appears in the dam downstream face (Fig. 21). These observations suggest that all the dams with different scaling factors exhibit essentially the same failure mode, i.e., the structural bending-induced tensile failure mode (Huang et al., 2020a, 2022a, 2022b). This is critical since it indicates that the deviations in dam failures are not produced due to different failure modes of dams.

The deviations in dam failures are then attributed mainly to the strain-rate effect. This can be substantiated as follows. Firstly, it has been verified that the strain rate of the small-scale model is $1/\beta$ times enhanced (Fig. 14) such that the small-scale model has been much

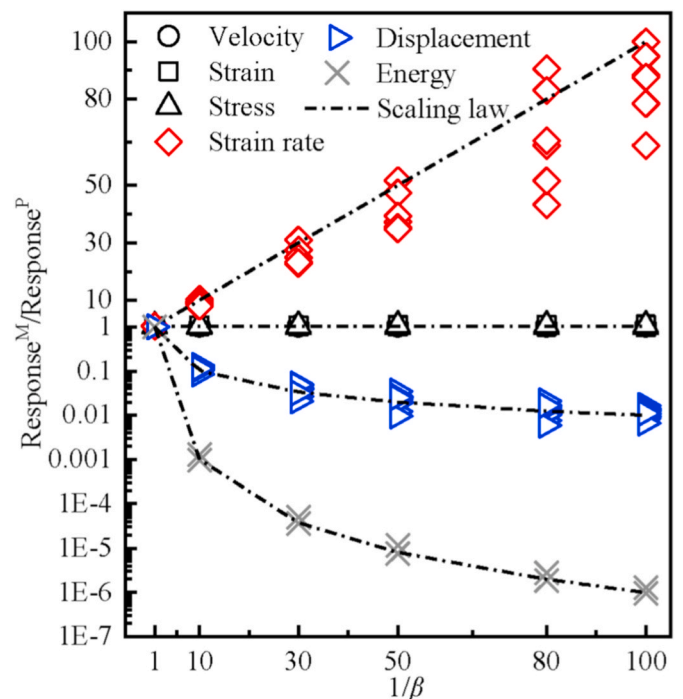


Fig. 18. Ratios of dam model responses to dam prototype responses.

strengthened (Fig. 15). Then, it is observed that with the increase of $1/\beta$, the dam failures are getting slighter, with the dam prototype being the most severely damaged (Fig. 20). Secondly, it is found that although the strain rate increases linearly with an increase of $1/\beta$ (Fig. 14), the increase in the DIF (Fig. 15) is rapid only at the beginning for the prototype and the small-scale model with $\beta = 1/10$, and is slow for models with smaller scaling factors. It is because the DIF grows slower and slower when the strain rate is sufficiently high and has an upper limit value, such as 10 for DIF_t and 2 for DIF_c of dry concrete (Eq. (10)). In this way, it is observed that the DIF_t for the small-scale models with $\beta = 1/30$, $1/50$, $1/80$, and $1/100$ are close and are strongly different from those for the prototype and the small-scale model with $\beta = 1/10$. Then, it is observed that the dam failure patterns of small-scale models with $\beta = 1/30$, $1/50$, $1/80$, and $1/100$ are almost identical and are different from those for the prototype and the small-scale model with $\beta = 1/10$. Thirdly, the dam upstream face in the z-direction is under tension, while the dam downstream face is under compression. The tensile behavior is sensitive to the strain rate, while the compressive behavior is not. Then, it is observed that the failures in the dam downstream face are almost

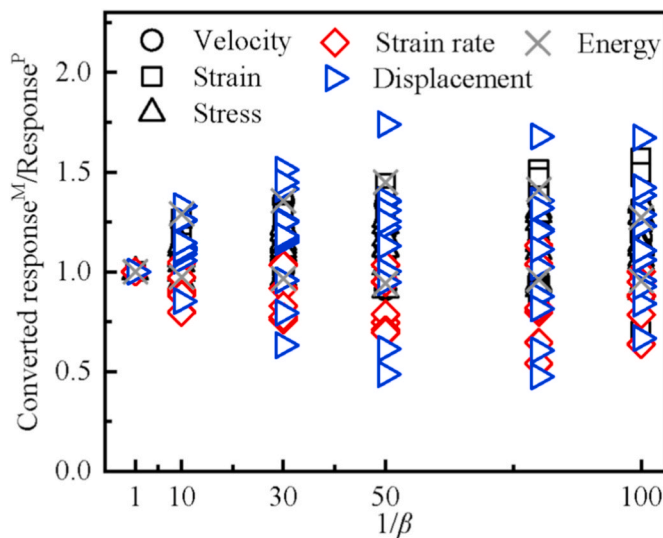


Fig. 19. Ratios of the converted dam model responses to dam prototype responses.

identical (Fig. 21), while for the dam upstream face, the dam failures of the prototype and the small-scale model with $\beta = 1/10$ are more severe than those with smaller scaling factors (Fig. 20). All these observations suggest that the strain-rate effect should be responsible for the deviations in dam failures.

It can be found that results in Sections 3.1 and 3.2 can draw a similar conclusion, i.e., when the strain-rate effect is prominent, such as in dam tensile stresses and tensile failures, the dimensional analysis-based scaling law in Table 1 is violated. Thus, corrected scaling laws with consideration of the strain-rate effect deserve more attention.

On the other hand, since the small-scale dam models are strengthened due to the enhanced strain rate, predictions of the dam failures by small-scale model tests with the uncorrected scaling law are conservative. However, from another point of view, the failures in the small-scale dam models indicate the most vulnerable positions of the dam. This

suggests that the small-scale model tests, despite the incomplete scaling law due to the strain-rate effect, can be used to identify the vulnerable positions of the dam prototype. This is critical since reinforcement measures beforehand can be applied to the identified vulnerable positions of the dam prototype to withstand the foreseeable attacks. For instance, in this study, for small-scale dam models with $\beta = 1/30, 1/50, 1/80,$ and $1/100,$ the dam failure patterns are almost identical with the appearance of two penetrating tensile fractures, one in the dam upper part and the other in the dam body (Fig. 20). Thus, the two positions are considered to be the most vulnerable positions of the dam prototype and need to be strengthened.

It was noted that some review literature (Chen et al., 2021; Wang et al., 2020a) had summarized the failures of real dams due to underwater explosions in historical wars. It was found that the failures of real gravity dams were observed as breaches with different depths in the dam upper part. In the current study with small-scale dam models, the failures of dam models were observed as penetrating fractures in the dam body. However, if the dam encountered a secondary attack, together with the upstream hydrostatic water pressure, similar breaches as those of real gravity dams can be expected in the dam model with the existence of penetrating fractures. This finding suggested that the failures of real dams and dam models were similar and thus consolidated the conclusions obtained in this study. Detailed comparisons and discussions of failures between real dams and dam models can be found in our previous study (Huang et al., 2020a).

5. Conclusions

In this study, the scaling of dynamic responses and failures of concrete gravity dams subjected to underwater explosion shock loadings has been investigated. The dimensional analysis-based scaling law, which is essentially the geometrical scaling law for dam structures and the Hopkinson scaling law for underwater explosion shock loadings, is adopted. Based on small-scale centrifuge tests, a numerical scheme that comprises six numerical simulations with geometrical scaling factor $\beta = 1, 1/10, 1/30, 1/50, 1/80,$ and $1/100$ is devised. The scaling of dam dynamic responses, including energy, velocity, displacement, strain, strain rate, and stress, is conducted, and similarities of dam failures are

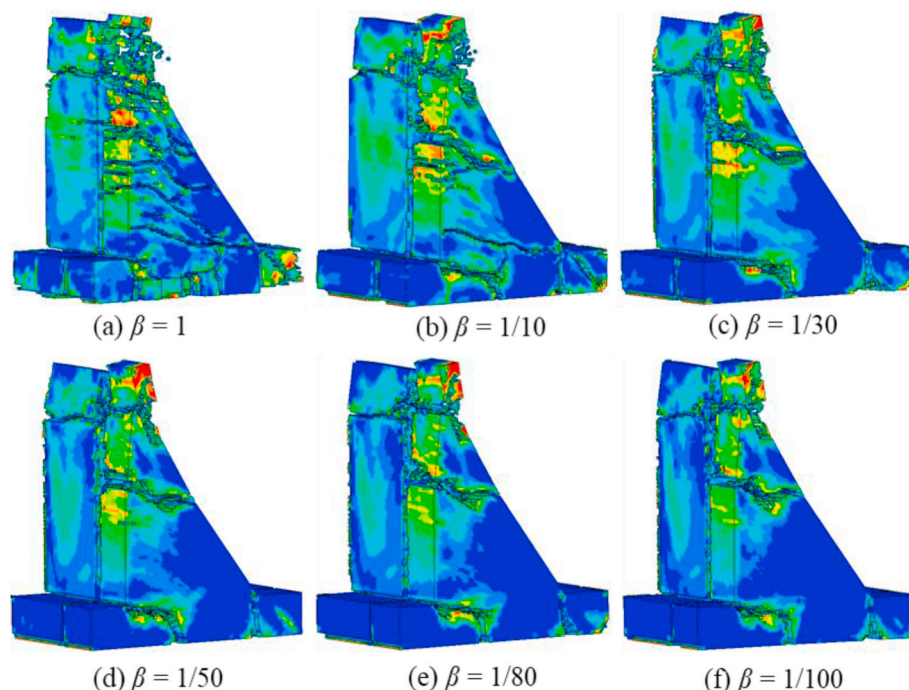


Fig. 20. Similarity of dam failures (upstream perspective).

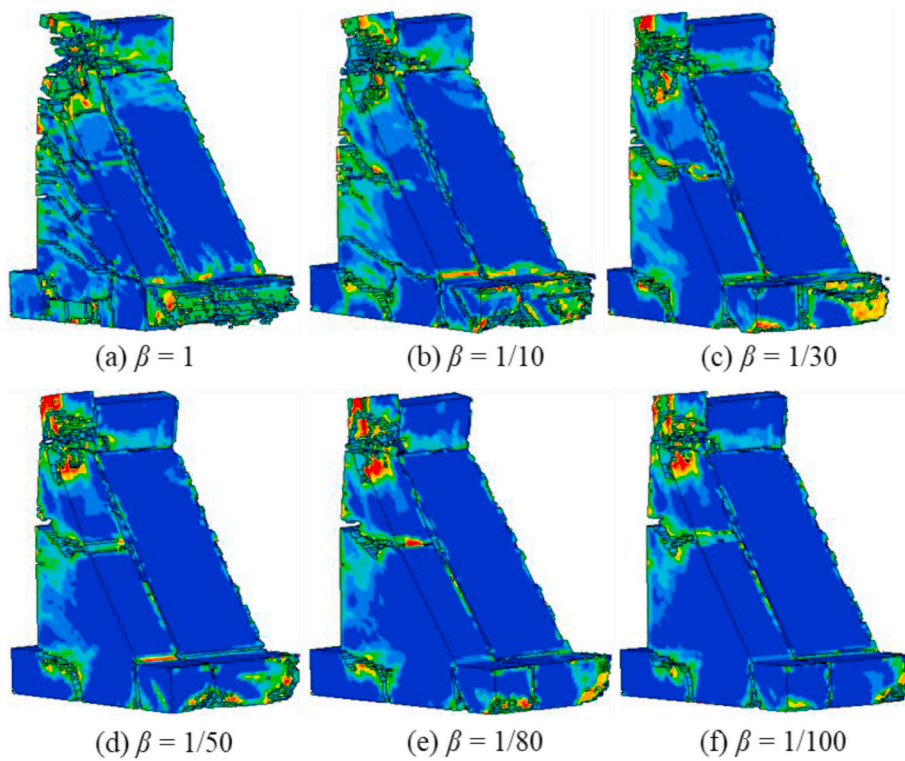


Fig. 21. Similarity of dam failures (downstream perspective).

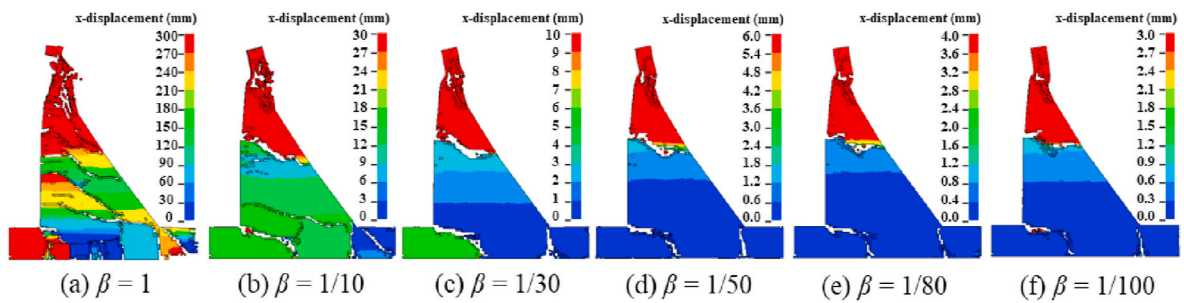


Fig. 22. Similarity of dam x-displacement fields.

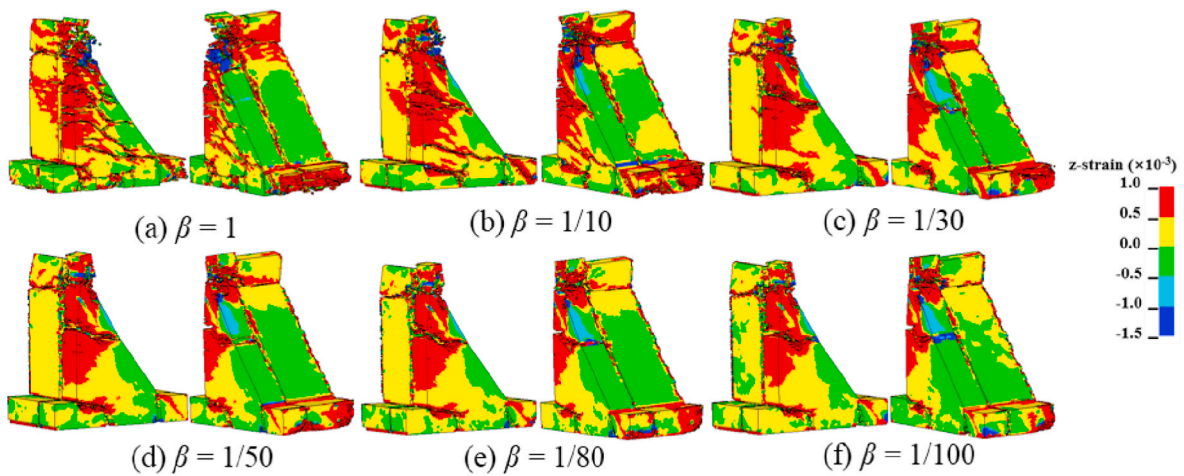


Fig. 23. Similarity of dam z-strain fields (negative strain denotes compression).

discussed. The strain-rate effect is highlighted. The major conclusions are summarized as follows.

- (1) The dam models with different scaling factors exhibit essentially the same failure mode, i.e., the structural bending-induced tensile failure mode. On this basis, most dam dynamic responses, including energy, velocity, displacement, strain, strain rate, and compressive stress, can well comply with the dimensional analysis-based scaling law.
- (2) The strain rate of the small-scale model is $1/\beta$ times enhanced. Therefore, when the strain-rate effect is pronounced, such as in dam tensile stresses and dam tensile failures, the dimensional analysis-based scaling law is violated. Corrected scaling law with consideration of strain-rate effect is required.
- (3) Due to enhanced strain rates of small-scale models, the dam failures are getting slighter as the scaling factor decreases, with the dam prototype the most severely destroyed. In particular, the dam failures for small-scale models with scaling factors $\beta = 1/30$, $1/50$, $1/80$, and $1/100$ are almost identical.
- (4) With the numerical scheme designed according to the dimensional analysis-based scaling law, the predictions of dam failures by small-scale model tests are conservative due to the strain-rate effect. However, from another point of view, the small-scale model tests, despite the incomplete scaling law, can be used to

identify the most vulnerable positions of the dam prototype. Then, reinforcement measures beforehand can be applied to the identified vulnerable positions of the dam prototype to withstand the foreseeable attacks.

CRediT authorship contribution statement

Xieping Huang: Investigation, Conceptualization, Methodology, Visualization, Formal analysis, Data curation, Writing – original draft, Writing – review & editing. **Xiangzhen Kong:** Validation, Funding acquisition, Software. **Jing Hu:** Data curation, Validation. **Qin Fang:** Funding acquisition, Software.

Declaration of competing interest

The authors declare that they have no known competing financial interests or personal relationships that could have appeared to influence the work reported in this paper.

Acknowledgments

This work was supported by the National Natural Science Foundations of China (grant nos. 52178515, 52078133, and 51879283).

Appendix A. Mesh convergence study

It is well known that the mesh size of the numerical model can influence the predictions by numerical simulations with the finite element method. In this study, a mesh size of 6 mm is adopted for the model scaled by a geometrical scaling factor $\beta = 1/80$, and the same mesh density is kept for the prototype and the other small-scale models. This mesh size has been examined previously (Huang et al., 2022a), where convergent results can be obtained for the small-scale model with $\beta = 1/80$. However, whether the same mesh density is suitable for the prototype and for the other small-scale models needs to be further verified. Thereby, a mesh convergence study in terms of the dam failures will be presented here.

It is trivially noted that the dam failures of small-scale models with scaling factors $\beta = 1/30$, $1/50$, $1/80$, and $1/100$ are almost identical (Figs. 20 and 21) and are different from those for the prototype and the small-scale model with $\beta = 1/10$. Thereby, the mesh convergence study can be conducted on the prototype and two small-scale models with $\beta = 1/10$ and $1/80$ as representative. Three different mesh densities are considered, named as coarse mesh, medium mesh, and finer mesh. Corresponding to the three different mesh densities, the mesh sizes of the small-scale model with $\beta = 1/80$ are 8, 6, and 4 mm, respectively, which according to the scaling law are 640, 480, 320 mm for the prototype, and 64, 48, 32 mm for the small-scale model with $\beta = 1/10$. The total elements for the three different mesh densities are 600737, 1259544, and 4048802, respectively.

Fig. A1 demonstrates the mesh size effect on the dam failures of the small-scale model with $\beta = 1/80$, while Fig. A2 for the prototype and Fig. A3 for the small-scale model with $\beta = 1/10$. It is observed that with three different mesh sizes, the dam failures are generally similar, which indicates that the predictions are not very sensitive to the mesh size. It can also be found that with medium mesh and finer mesh, the dam failures are almost the same (Figs. A1, A2, and A3), which indicates that convergent results can be obtained with the medium mesh. These findings suggest that the mesh size employed in this study is appropriate and will not affect the conclusions obtained.

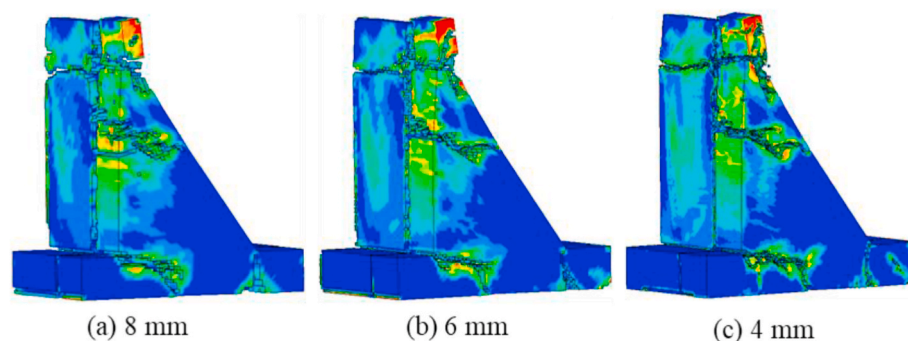


Fig. A1. Mesh size effect on dam failures of small-scale model with scaling factor $\beta = 1/80$

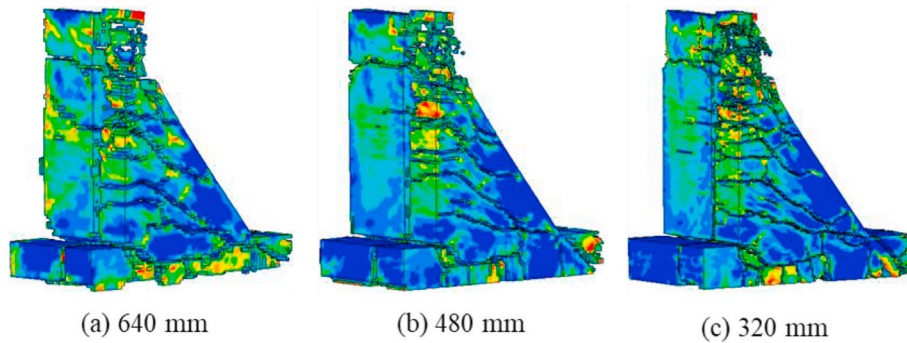


Fig. A2. Mesh size effect on dam failures of the prototype

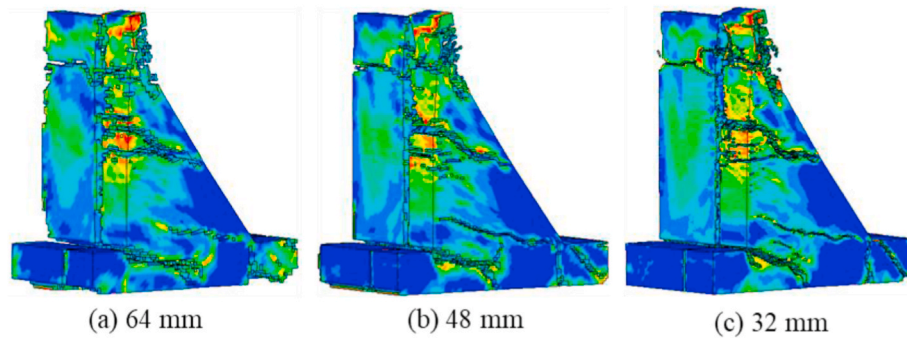


Fig. A3. Mesh size effect on dam failures of small-scale model with scaling factor $\beta = 1/10$

Appendix B. Similarity of dam failures based on centrifuge test UE-02

To enrich the results and consolidate the conclusions in this study, another numerical scheme with the inclusion of six numerical simulations is designed, which is based on the centrifuge test UE-02. As presented in Table B1, the numerical simulation SUE-10 is the simulation of centrifuge test UE-02, and the other five numerical simulations are then designed based on the scaling law (Table 1). It should be noted that the scaled distance in this scheme is maintained near $0.9687 \text{ m/kg}^{1/3}$, which is quite larger than that in Table 4. Hence, the dam failures will be slighter. Fig. B1 compares the dam failures. It is observed that for small-scale models with $\beta = 1/10, 1/30, 1/50, 1/80,$ and $1/100$, the dam failures are almost identical, where only the dam upper part is severely destroyed with a horizontal fracture visible along the dam downstream slop. However, by inspections of the failures in the dam bottom, it can be found that the dam failures are getting more and more severe with an increase of $1/\beta$. The dam prototype is the most severely damaged, where dam failures concentrate not only on the dam upper part, but also on the dam body with the appearance of two penetrating fractures. These findings are similar to those for Table 4, as presented in Section 3.2, and thus the conclusions are consolidated.

Table B1
Numerical scheme based on centrifuge test UE-02

Parameters	No.					
	Prototype	Model				
	SUE-07	SUE-08	SUE-09	SUE-10	SUE-11	SUE-12
Scaling factor/ β	1	1/10	1/30	1/50	1/80	1/100
Acceleration of gravity/ ng	1	10	30	50	80	100
Dam height, h/m	27.5	2.75	0.917	0.55	0.344	0.275
Water depth, H_w/m	30	3	1	0.6	0.375	0.3
Standoff distance, R_c/m	5	0.5	0.167	0.1	0.0625	0.05
Detonation depth, L/m	5	0.5	0.167	0.1	0.0625	0.05
Explosive weight, W/kg	137.5	0.1375	5.09×10^{-3}	1.1×10^{-3}	0.27×10^{-3}	0.1375×10^{-3}
Scaled distance, $Z = R_c/W^{1/3}/m/kg^{1/3}$	0.9687	0.9687	0.9708	0.9687	0.9670	0.9687

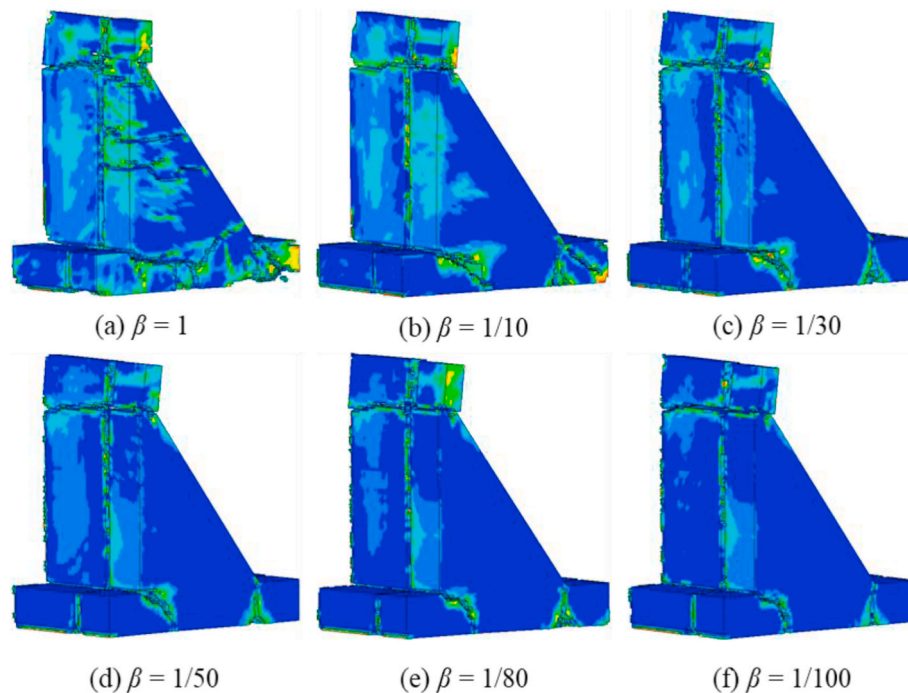


Fig. B1. Similarity of dam failures

References

- Alves, M., 2020. *Impact Engineering: Fundamentals, Experiments and Nonlinear Finite Elements*. <https://doi.org/10.4322/978-85-455210-0-6>.
- Baker, W.E., 1973. *Explosions in Air*. University of Texas Press, Austin, TX, USA.
- Baker, W.E., Westine, P.S., Dodge, F.T., 1973. *Similarity Methods in Engineering Dynamics*. Hayden Book Company, Inc., New Jersey, pp. 113–142.
- Cadoni, E., Labibes, K., Albertini, C., Berra, M., Giangrosso, M., 2001. Strain-rate effect on the tensile behavior of concrete at different relative humidity levels. *Mater. Struct.* 34, 21–26.
- Chen, J.Y., Liu, X.P., Xu, Q., 2017. Numerical simulation analysis of damage mode of concrete gravity dam under close-in explosion. *KSCE J. Civ. Eng.* 21 (1), 397–407.
- Chen, Y.Q., Lv, L.M., Wang, G.H., Lu, W.B., 2021. Review on the blast-resistance performance evaluation of dams. *China Civ. Eng. J.* 54 (10), 9–19 (In Chinese).
- Cole, R.H., 1948. *Underwater Explosions*. Princeton University Press, New Jersey.
- Ferguson, G.L., 1995. Replica model scaling for high strain-rate events. *Int. J. Impact Eng.* 16 (4), 571–583.
- Fu, S., Gao, X., Chen, X., 2018. The similarity law and its verification of cylindrical lattice shell model under internal explosion. *Int. J. Impact Eng.* 122, 38–49.
- Fu, T., Zhang, M., Zheng, Q., Zhou, D., Sun, X., Wang, X., 2021. Scaling the response of armor steel subjected to blast loading. *Int. J. Impact Eng.* 153, 103863.
- Huang, X.P., Hu, J., Zhang, X.D., Zhang, Z.T., Kong, X.Z., 2020a. Bending failure of a concrete gravity dam subjected to underwater explosion. *J. Zhejiang Univ. - Sci.* 21 (12), 976–991.
- Huang, X.P., Kong, X.Z., Hu, J., Zhang, X.D., Zhang, Z.T., Fang, Q., 2020b. The influence of free water content on ballistic performances of concrete targets. *Int. J. Impact Eng.* 139, 103530.
- Huang, X.P., Kong, X.Z., Chen, Z.Y., Fang, Q., Peng, Y., 2020c. Equation of state for saturated concrete: a mesoscopic study. *Int. J. Impact Eng.* 144, 103669.
- Huang, X.P., Hu, J., Zhang, X.D., Zhang, Z.T., 2022a. Effect of bubble pulse on concrete gravity dam subjected to underwater explosion: centrifuge test and numerical simulation. *Ocean. Eng.* 243, 110291.
- Huang, X.P., Kong, X.Z., Hu, J., Fang, Q., 2022b. Failure modes of concrete gravity dam subjected to near-field underwater explosion: centrifuge test and numerical simulation. *Eng. Fail. Anal.* 137, 106243.
- Hu, J., Chen, Z.Y., Zhang, X.D., Wei, Y.Q., Liang, X.Q., Liang, J.H., Ma, G.W., Wang, Q.S., Long, Y., 2017. Underwater explosion in centrifuge part I: validation and calibration of scaling laws. *Sci. China Technol. Sci.* 60 (11), 1638–1657.
- Jones, N., 2012. *Structural Impact*, second ed. Cambridge University Press, Cambridge.
- Kong, X.S., Li, X., Zheng, C., Liu, F., Wu, W.G., 2017. Similarity considerations for scale-down model versus prototype on impact response of plates under blast loads. *Int. J. Impact Eng.* 101, 32–41.
- Kong, X.Z., Fang, Q., Chen, L., Wu, H., 2018. A new material model for concrete subjected to intense dynamic loadings. *Int. J. Impact Eng.* 120, 60–78.
- Li, Q., Wang, G.H., Lu, W., Niu, X., Chen, M., Yan, P., 2018a. Influence of reservoir water levels on the protective performance of concrete gravity dams subjected to underwater explosions. *J. Struct. Eng.* 144 (9), 04018143.
- Li, Q., Wang, G.H., Lu, W.B., Niu, X.Q., Chen, M., Yan, P., 2018b. Failure modes and effect analysis of concrete gravity dams subjected to underwater contact explosion considering the hydrostatic pressure. *Eng. Fail. Anal.* 85, 62–76.
- Mazzariol, L.M., Oshiro, R.E., Alves, M.A., 2016. A method to represent impacted structures using scaled models made of different materials. *Int. J. Impact Eng.* 90, 81–94.
- Lu, L., Li, X., Zhou, J., 2014. Study of damage to a high concrete dam subjected to underwater shock waves. *Earthq. Eng. Vib.* 13 (2), 337–346.
- Magnus, D., Khan, M.A., Proud, W.G., 2018. Epidemiology of civilian blast injuries inflicted by terrorist bombings from 1970–2016. *Defence Technol.* 14 (5), 469–476.
- Malecot, Y., Zingg, L., Briffaut, M., Baroth, J., 2019. Influence of free water on concrete triaxial behavior: the effect of porosity. *Cement Concr. Res.* 120, 207–216.
- Neuberger, A., Peles, S., Rittel, D., 2007. Scaling the response of circular plates subjected to large and close-range spherical explosions. Part I: air-blast loading. *Int. J. Impact Eng.* 34 (5), 859–873.
- Noam, T., Dolinski, M., Rittel, D., 2014. Scaling dynamic failure: a numerical study. *Int. J. Impact Eng.* 69, 69–79.
- Oshiro, R.E., Alves, M., 2004. Scaling impacted structures. *Arch. Appl. Mech.* 74 (1), 130–145.
- Oshiro, R.E., Calle, M.A.G., Mazzariol, L.M., Alves, M., 2017. Experimental study of collision in scaled naval structures. *Int. J. Impact Eng.* 110, 149–161.
- Ramamurthi, K., 2021. *Modeling Explosions and Blast Waves*, ISBN 978-3-030-74337-6.
- Ren, X.B., Huang, Z.X., Jiang, Y.B., Chen, Z.H., Cao, X.F., Zhao, T., Li, Y., 2022. The scaling laws of cabin structures subjected to internal blast loading: experimental and numerical studies. *Def. Technol.* 18 (5), 811–822.
- Ren, X.D., Shao, Y., 2019. Numerical investigation on damage of concrete gravity dam during noncontact underwater explosion. *J. Perform. Constr. Facil.* 33 (6), 04019066.
- Rossi, P., 1991. A physical phenomenon which can explain the mechanical behavior of concrete under high strain rates. *Mater. Struct.* 24 (6), 422–424.
- Saadatfar, S., Zahmatkesh, A., 2018. Evaluation of underwater blast on concrete gravity dams using three-dimensional finite-element model. *AUT J. Civil. Eng.* 2 (1), 69–78.
- Snyman, I.M., 2010. Impulsive loading events and similarity scaling. *Eng. Struct.* 32 (3), 886–896.
- U.S. Department of Homeland Security, 2012. *Worldwide Attacks against Dams-A Historical Threat Resource for Owners and Operators*. U.S. Department of Homeland Security, Washington D.C., 2012.
- Vanadit-Ellis, W., Davis, L.K., 2010. Physical modelling of concrete gravity dam vulnerability to explosions. In: *2010 International Water Side Security Conference*, pp. 1–11.
- Wang, C., Wei, P.Y., Wang, X.H., Zhang, S.R., Cui, W., 2021. Blast-resistance and damage evaluation of concrete gravity dam exposed to underwater explosion: considering the initial stress field. *KSCE J. Civ. Eng.* 25, 2922–2935.

- Wang, G.H., Zhang, S.R., 2014. Damage prediction of concrete gravity dams subjected to underwater explosion shock loading. *Eng. Fail. Anal.* 39, 72–91.
- Wang, G.H., Zhang, S.R., Kong, Y., Li, H.B., 2015. Comparative study of the dynamic response of concrete gravity dams subjected to underwater and air explosions. *J. Perform. Constr. Facil.* 29 (4), 04014092.
- Wang, G.H., Lu, W.B., Yang, G.D., Yan, P., Chen, M., Zhao, X.H., Li, Q., 2020a. A state-of-the-art review on blast resistance and protection of high dams to blast loads. *Int. J. Impact Eng.* 139, 103529.
- Wang, W., Zhang, D., Lu, F., Wang, S.C., Tang, F., 2012. Experimental study on scaling the explosion resistance of a one-way square reinforced concrete slab under a close-in blast loading. *Int. J. Impact Eng.* 49, 158–164.
- Wang, X.H., Zhang, S.R., Wang, C., Cui, W., Cao, K.L., Fang, X., 2020b. Blast-induced damage and evaluation method of concrete gravity dam subjected to near-field underwater explosion. *Eng. Struct.* 209, 109996.
- Xu, H., Wen, H.M., 2013. Semi-empirical equations for the dynamic strength enhancement of concrete-like materials. *Int. J. Impact Eng.* 60, 76–81.
- Yao, S., Zhang, D., Lu, F., Chen, X., Zhao, P., 2017. A combined experimental and numerical investigation on the scaling laws for steel box structures subjected to internal blast loading. *Int. J. Impact Eng.* 102, 36–46.
- Yao, S., Ma, Y., Zhao, N., Wang, Z., Zhang, D., Lu, F., 2022. Equivalent scaling method on the dynamic response of box-shaped structures under internal blast. *Int. J. Impact Eng.* 160, 104074.
- Zhang, S.R., Wang, G.H., Wang, C., Pang, B.H., Du, C.B., 2014. Numerical simulation of failure modes of concrete gravity dams subjected to underwater explosion. *Eng. Fail. Anal.* 36, 49–64.
- Zhao, F.Q., Wen, H.M., 2018. Effect of free water content on the penetration of concrete. *Int. J. Impact Eng.* 121, 180–190.
- Zhang, Q.L., Hu, Y.G., Liu, M.S., Li, D.Y., 2021. Role of negative pressure in structural responses of gravity dams to underwater explosion loadings: the need to consider local cavitation. *Eng. Fail. Anal.* 122, 105270.